

AD-A104 578

HARRY DIAMOND LABS ADELPHI MD

F/G 20/6

THE DECONVOLUTION OF AEROSOL BACKSCATTERED OPTICAL PULSES TO 08--ETC(U)

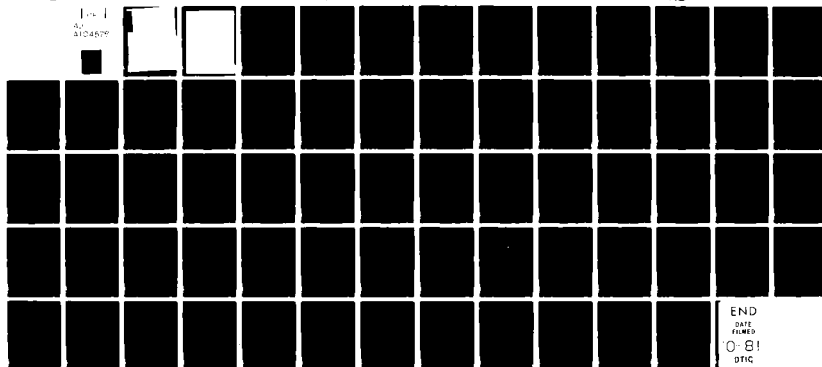
JUN 81 D MCGUIRE, M. CONNER

UNCLASSIFIED

HDL-TR-1944

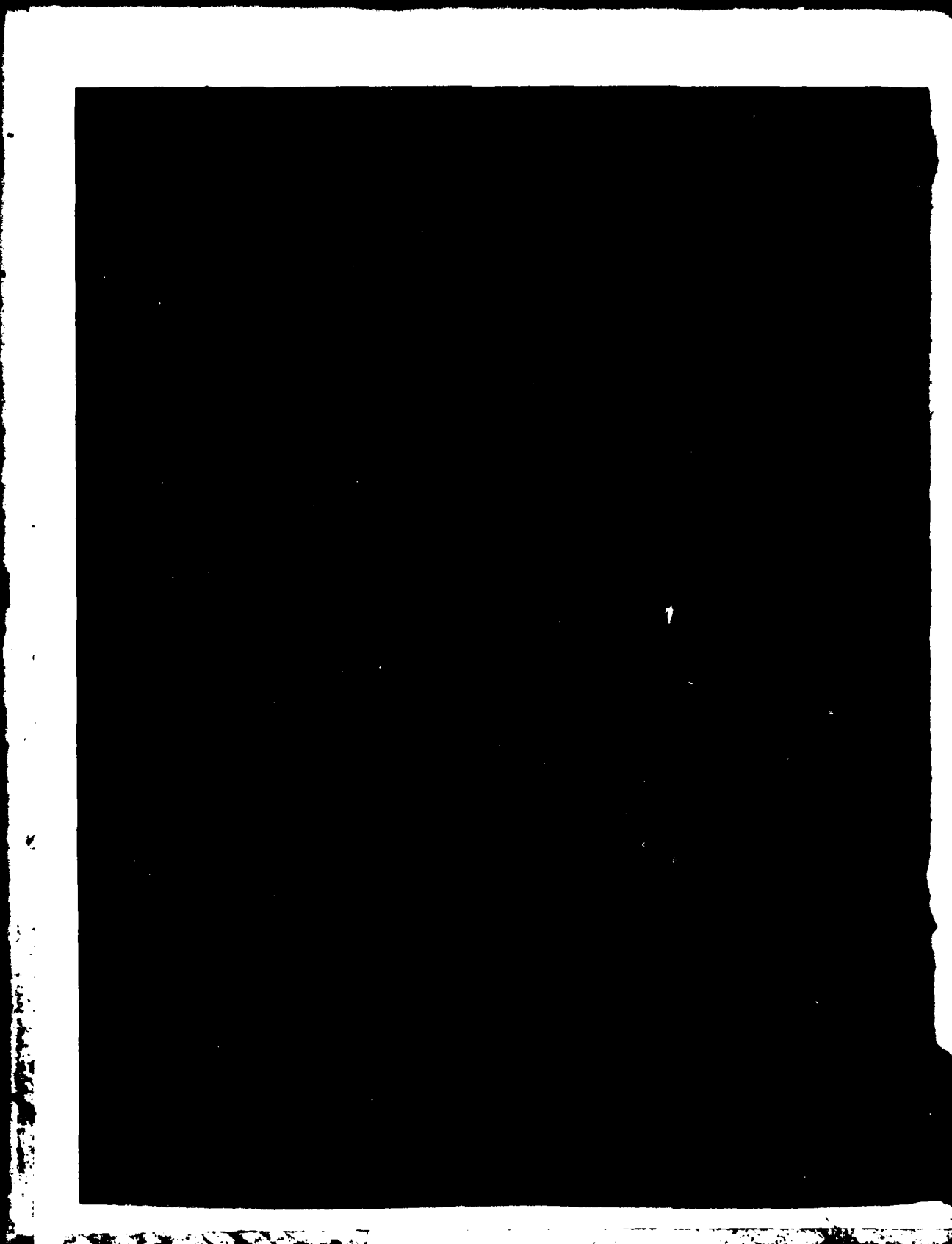
NL

Doc 1  
AL  
3104679



END  
DATE  
FILMED  
0-81  
DTIC

ADA104578



UNCLASSIFIED

SECURITY CLASSIFICATION OF THIS PAGE (When Data Entered)

REPORT DOCUMENTATION PAGE		READ INSTRUCTIONS BEFORE COMPLETING FORM
1. REPORT NUMBER HDL-TR-1944	2. GOVT ACCESSION NO. AD-A104578	3. RECIPIENT'S CATALOG NUMBER
4. TITLE (and Subtitle) The Deconvolution of Aerosol Back-scattered Optical Pulses to Obtain System-Independent Aerosol Signatures.		5. TYPE OF REPORT & PERIOD COVERED Technical Report.
7. AUTHOR(s) Dennis McGuire Michael/Conner		6. PERFORMING ORG. REPORT NUMBER
9. PERFORMING ORGANIZATION NAME AND ADDRESS Harry Diamond Laboratories 2800 Powder Mill Road Adelphi, MD 20783		8. CONTRACT OR GRANT NUMBER(s)
11. CONTROLLING OFFICE NAME AND ADDRESS Commander U.S. Army ARRADCOM Dover, NJ 07801		10. PROGRAM ELEMENT, PROJECT, TASK AREA & WORK UNIT NUMBERS Program Ele.: MAIF
14. MONITORING AGENCY NAME & ADDRESS (if different from Controlling Office)		12. REPORT DATE June 1981
		13. NUMBER OF PAGES 66
		15. SECURITY CLASS. (of this report) UNCLASSIFIED
		15a. DECLASSIFICATION/DOWNGRADING SCHEDULE
16. DISTRIBUTION STATEMENT (of this Report)  Approved for public release; distribution unlimited.		
17. DISTRIBUTION STATEMENT (of the abstract entered in Block 20, if different from Report)		
18. SUPPLEMENTARY NOTES HDL Project: A18032 DRCMS Code: 36KA5000204		
19. KEY WORDS (Continue on reverse side if necessary and identify by block number) Aerosol backscatter      Optical fuzing Deconvolution              Active optical sensors		
20. ABSTRACT (Continue on reverse side if necessary and identify by block number) Means are discussed for extracting system-independent aerosol signatures from aerosol backscatter measurements obtained with a specific pencil beam active optical detection system. Such signatures are required before the backscatter data can be applied to various proposed optical fuze designs for determining their aerosol vulnerability and to the investigation of aerosol discrimination schemes. The measurement system, which has been		

DD FORM

1 JAN 73

1473

EDITION OF 1 NOV 65 IS OBSOLETE

UNCLASSIFIED

SECURITY CLASSIFICATION OF THIS PAGE (When Data Entered)

UNCLASSIFIED

SECURITY CLASSIFICATION OF THIS PAGE(When Data Entered)

20. ABSTRACT (Cont'd)

used in numerous experiments to probe such aerosols as weather clouds and military smokes, is a short pulse GaAs laser probe (pulse width  $\leq 10$  ns) whose range sensitivity extends from near the system to beyond 10 m.

The resolution needed for realistic evaluations of aerosol density gradient effects on optical fuzing systems is greater than that inherent in the spatial width of the probing pulses, which is approximately 2 m. To achieve such superresolution requires analytical and numerical techniques to deconvolve the transmitted pulses from the signatures. Deconvolution methods are investigated for measurement noise conditions typical of the backscatter data. A computationally fast numerical deconvolution algorithm is devised together with a comprehensive supporting analysis. Both indicate that severe signal-to-noise ratio constraints apply to the achievement of meaningful superresolution.

While the signal-to-noise ratios typical of recent measurements are likely to satisfy the severe constraints discovered, many of the earlier data are too noisy and thus require other signature determination methods. An alternative approach is discussed and given a preliminary evaluation. The approach, which seems promising, involves the use of a priori knowledge of the nature of the signature coupled with parameter estimation techniques.

<b>Accession For</b>	
NTIS GRA&I	<input checked="" type="checkbox"/>
DTIC TAB	<input type="checkbox"/>
Unannounced	<input type="checkbox"/>
Justification	
By	
Distribution/	
Availability Codes	
Dist	Avail and/or Special
A	

DTIC  
ELECTE  
S SEP 20 1981  
D

RE: Classified References, Distribution Unlimited  
No change in distribution statement per Mr. Dennis McGuire, HDL/DELHD-RT-CB

UNCLASSIFIED

2 SECURITY CLASSIFICATION OF THIS PAGE(When Data Entered)

## CONTENTS

	<u>Page</u>
1. INTRODUCTION.....	7
2. PRELIMINARY DISCUSSION OF SIGNATURE EXTRACTION PROBLEM.....	11
2.1 Linear System Description.....	11
2.2 Typical Transmitter Pulses, Range Law, and Signatures.....	12
3. FORMAL AND NUMERICAL SOLUTIONS OF DECONVOLUTION PROBLEM.....	20
3.1 Formal Solution and Effect of Noise.....	20
3.2 Numerical Deconvolution.....	23
3.2.1 Discrete Formulation.....	23
3.2.2 Z-Transform Deconvolution.....	25
4. EFFECT OF NOISE IN SIGNATURE EXTRACTION.....	31
4.1 Numerical Effect.....	31
4.2 Analytical Estimation of Noise Effects.....	33
5. ALTERNATIVE APPROACH THROUGH PARAMETER ESTIMATION.....	44
5.1 Estimation of $\sigma$ and $\mu$ for Uniform Aerosol.....	46
5.2 Estimation of $\sigma$ and $\mu$ from Measured Return Signals.....	51
6. SUMMARY AND DISCUSSION.....	60
LITERATURE CITED.....	63
DISTRIBUTION.....	65

# FIGURES

	<u>Page</u>
1 Shape of typical optical pulse from GaAs laser pulser.....	13
2 Shape of typical optical pulse from improved GaAs laser pulser.....	14
3 Measured range-response curve, $R(x)$ , of pencil beam GaAs laser probe for aerosol backscatter measurements.....	15
4 Illustration of idealized aerosol density profile along pencil beam influence pattern of active optical detection system.....	17
5 Aerosol signatures calculated from defining equation (1) for aerosol density profile.....	18
6 Aerosol signature for semi-infinite uniform aerosol distribution.....	19
7 Computed aerosol signature according to equations (6) and (7).....	27
8 Product of aerosol signature of figure 7 and range-response function computed from equation (29).....	28
9 Computed aerosol return signal according to equation (23).....	29
10 Product of aerosol signature and range response function.....	30
11 Result of deconvolving return signal of figure 9.....	32
12 Comparison of shape of model transmitter pulse with that of measured transmitter pulse of figure 2.....	34
13 Sketch of graph of $I(x) = (\pi x)^2 (1 - x^2)^2 / \sin^2 \pi x$ .....	36
14 Sketch of graph of $J(x_c) = \int_0^{x_c} I(x) dx$ versus $x_c$ and versus $f_c = x_c / 2T$ .....	38
15 Signal-to-noise ratio penalty factor for model transmitter pulse of equation (32).....	42
16 Signal-to-noise ratio penalty factor for measured transmitter pulse of figure 2.....	43

FIGURES (Cont'd)

	<u>Page</u>
17 Constant-cost contours of $J(\sigma, \mu)$ .....	48
18 Typical trajectories for steepest descent algorithm.....	49
19 Typical trajectories for intuitive algorithm.....	50
20 Sampled values of measured cumulus cloud return signal.....	52



## 1. INTRODUCTION

A measurement program that collects laser backscatter data from various aerosols and simultaneously makes measurements to characterize the aerosol environment has been underway at the Harry Diamond Laboratories (HDL) for several years. Measurements have been made on water clouds during helicopter flight tests and on other aerosols such as smoke, dust, and fog. The purpose of these measurements has been largely to furnish the data needed to determine aerosol backscatter effects on active optical fuzing (AOF) systems using GaAs injection laser transmitters, since such effects could cause false target problems. This report discusses the results of several related investigations whose purpose was to provide the needed interpretations of the backscatter data and the methods by which the data can be used to determine aerosol backscatter effects in various proposed AOF systems. The measurement program itself is discussed fully by McGuire, Smalley, and Sztankay.<sup>1-3</sup>

The methods used for backscatter signal acquisition and subsequent digitization of the data are discussed in detail by Vanderwall and Conner.<sup>4</sup> The data, a train of received signal pulses, are recorded during the measurements on video tape in standard television (TV) format so that each TV frame contains the data for an entire backscattered pulse. A specially designed electronic frame-code generator applies a sequential code number to each TV frame during the data recording. By using another specially designed device, the coded video tape data are automatically digitized in our laboratory and thereby put in a form suitable for further processing and analysis by computer.

The immediate question for data usage concerns how backscatter data obtained with a particular active optical detection system--the measurement system employs a GaAs short-pulse laser probe--can be translated to apply to another system that might differ from the first in such respects as range coverage and transmitter pulse characteristics. An answer can be formulated in terms of an aerosol signature concept, provided that multiple scattering contributions to the aerosol return signals can be ignored.

<sup>1</sup>D. McGuire, H. M. Smalley, and Z. G. Sztankay, *Measurements of Backscatter Effects in Clouds at 0.9  $\mu$ m (U)*, Proc. JTCG/MD/WPFF Tri-Service Optical Fuze Technology Symposium, Naval Weapons Center NWC TP 5871, Part I (October 1976), 45-74. (CONFIDENTIAL)

<sup>2</sup>Z. G. Sztankay and D. McGuire, *Backscatter in Clouds at 0.9  $\mu$ m and Its Effects on Optical Fuzing Systems (U)*, Proc. Seventh DoD Conference on Laser Technology (November 1977). (SECRET)

<sup>3</sup>Z. G. Sztankay, *Measurement of the Localized Optical Characteristics of Natural Aerosols, Smoke, and Dust*, Proc. Smoke/Obscurants Symposium II (25-26 April 1979).

<sup>4</sup>Jonathan Vanderwall and Michael Conner, *A Novel Scan-Converting Oscillographic Technique for In-Situ Signal Acquisition with Subsequent Automatic Digitization*, Harry Diamond Laboratories HDL-TR-1956 (1981).

To develop the aerosol signature concept, consider first the GaAs laser probe used to collect the backscatter data. It is a pencil beam active optical detection system employing a short-pulse GaAs injection laser transmitter and a transceiver influence pattern sensitive from ranges near the system out to ranges in excess of 10 m. The transmitter pulse widths, measured by the full width at half maximum (FWHM), are currently 5 ns, but many of the data were obtained with wider pulses (7 and 11 ns FWHM) using earlier versions of the probe. The shape of the detected aerosol return pulses depends on several factors besides the distribution of aerosol in the influence pattern. These factors include the shape of the transmitter pulses and the shape of the range sensitivity curve of the system.

The foregoing dependencies can be expressed in a useful mathematical form with the aid of the following definitions. Let  $P(t)$  and  $V(t)$  be the instantaneous transmitted power and return signal, respectively, and let  $x$  denote range from the transceiver measured along its pencil beam influence pattern. Define the function of range  $C(x)$  by

$$C(x) = \mu(x) \exp \left[ -2 \int_0^x \sigma(s) ds \right], \quad (1)$$

where  $\mu(x)$  and  $\sigma(x)$  are, respectively, the volume backscatter and extinction coefficients of the aerosol at range  $x$ . Finally, let  $R(x)$  denote the range sensitivity function of the system. (The function  $R$  is defined as the peak receiver response to a flat reflecting target, oriented at right angles to and filling the influence pattern, as a function of range from the transceiver to the target. The scale of values of  $R$  depends on the units of receiver response and the target reflectivity; ordinarily, some convenient normalization of the scale is used.) Then  $V(t)$  can be expressed as

$$V(t) = K \int_0^\infty P(t-\tau) C(c\tau/2) R(c\tau/2) d\tau, \quad (2)$$

provided that the receivers respond linearly to the received optical power; the factor  $K$  is a constant depending on the normalization chosen for  $R(x)$  and the units of  $V(t)$ ;  $c$  is the speed of light. This result, originally derived by Burroughs,<sup>5</sup> has considerable generality; it applies not only to the GaAs laser probe, but to virtually all pencil

<sup>5</sup>H. H. Burroughs, *Computation of Cloud Backscatter Power as a Function of Time for an Active Optical Radar (U)*, Naval Weapons Center NWC TP 5090 (April 1971). (CONFIDENTIAL)

beam active optical detection systems where transmitter and receiver are approximately collocated. However, multiple scattering effects are ignored in deriving equation (2).

To see the usefulness of equation (2) more fully, suppose that a pencil beam system satisfying the general requirements of the previous paragraph is operating in an aerosol environment and that it is desired to calculate the aerosol return signal. Assuming that the aerosol distribution is known in terms of its extinction and backscatter coefficients, equation (1) can be used to calculate the function  $C(x)$  once the location of the transceiver and the orientation of its pencil beam influence pattern relative to the aerosol distribution are specified. Knowledge of the range sensitivity curve and the instantaneous transmitted power then permits the calculation of the desired return signal by using equation (2).  $C(x)$  is system independent, being determined solely by the aerosol distribution and the encounter geometry. For this reason,  $C(x)$  is referred to here as the aerosol signature (for a given encounter).

The aerosol signature concept easily extends to wide angle influence pattern systems, since these can be viewed as superpositions of many pencil beam systems; however, it is unlikely that multiple scattering effects can be ignored altogether in the wide angle case. To the extent that such effects can be ignored, the aerosol signature concept provides a solution to the problem being considered, namely, how backscatter data obtained with the GaAs laser probe can be made to apply to AOF systems with a different influence pattern and different transmitter pulse characteristics. One needs to extract the aerosol signatures,  $C$ , contained in the measured aerosol return signals,  $V$ , these being related according to equation (2), with  $K$ ,  $P$ , and  $R$  understood to refer to the GaAs laser probe. The investigations to be discussed in this report are concerned mainly with how to accomplish the signature extraction.

There is a simple approximate way to determine the aerosol signature from the measured return signal. The laser probe features short transmitter pulses (5 to 11 ns FWHM) and is sensitive to aerosol over a range interval (in excess of 10 m) consistent with fuzing applications. If one approximates the transmitter pulse by a temporal  $\delta$ -function, then equation (2) shows that the return signal is proportional to the product of the aerosol signature and the probe's range response function. Thus the aerosol signature can be obtained approximately by dividing the return signal values (expressed as a function of range using the transformation  $t \rightarrow 2x/c$ ) by the corresponding values of the range response function, appropriately scaled. This approximate determination sacrifices resolution in the resulting  $C(x)$ . Since the spatial width of the transmitter pulse is about 2 m, the  $C(x)$  obtained will be smeared relative to the actual  $C(x)$  by a spatial average over about a 2-m interval.

The general signature extraction problem is basically to solve equation (2) as an integral equation for  $C(x)$ , given  $V(t)$ ,  $P(t)$ , and  $R(x)$ , and to analyze the errors produced in the solution by the noise accompanying  $V(t)$ . In section 2, the problem is formulated as one of deconvolution, that is, inverting a convolution operator, and a useful point of view for analyzing noise effects is indicated. In addition, the transmitter pulses and range-response function of the GaAs probe are described, and a number of idealized aerosol signatures are computed and displayed graphically.

In section 3, a formal solution of the deconvolution problem is given in terms of Fourier transforms, and a formulation of the noise analysis problem is developed on the basis of the formal solution. Then a method is presented for the numerical solution of equation (2) involving the use of the discrete Z-transform. This method leads to a highly efficient and accurate solution algorithm. A sample computation illustrating the accuracy is given.

Section 4 completely analyzes the noise induced errors in the general signature extraction process. As might be expected, the critical factors for such errors are the width and the shape of the transmitter pulse. By making reasonable assumptions about the statistics of the noise present in the backscatter data, the errors in determining  $C(x)$  by deconvolution can be expressed in the form of a signal-to-noise ratio (SNR). The SNR of  $C(x)$  is calculated for a transmitter pulse that much of the backscatter data were obtained with; the pulse is somewhat asymmetrical (the leading edge is faster than the trailing edge) and measures 7 ns FWHM. This calculation was performed by assuming that the backscatter data were bandpass filtered with various upper frequency cutoffs so that the effect of data smoothing could be studied. The results show that the data in question cannot be profitably treated with the deconvolution method because the SNR's of  $C(x)$  are unacceptably low for reasonable amounts of data smoothing and the typical SNR of the backscatter data (about 15:1, peak signal to rms noise).

The foregoing negative conclusions do not apply to backscatter data that are now being obtained (and that were unavailable when this study was conducted). The current data are being obtained with a shorter (5 ns FWHM), more nearly symmetrical transmitter pulse that has considerably more peak power than was previously available. The combination of increased SNR for the backscatter data and changed temporal characteristics of the transmitter pulse could make the deconvolution method useful for the newer data. Some speculation along these lines is offered in section 6.

A preliminary discussion is given in section 5 of an alternative strategy for accomplishing signature extraction. This strategy involves the use of a priori knowledge about the signature and parameter estimation techniques.

## 2. PRELIMINARY DISCUSSION OF SIGNATURE EXTRACTION PROBLEM

Before considering methods for signature extraction, it is useful to express the ideas surrounding equation (2) in the language of linear system theory and to describe in more detail the several functions-- $P(t)$ ,  $R(x)$ , and  $C(x)$ --that enter into the problem.

### 2.1 Linear System Description

Equation (2) can be seen to express  $V(t)$  as a convolution integral if the convention is adopted of putting  $C$  and  $R$  equal to zero for negative values of their arguments. Then the lower limit on the integral can be changed to  $-\infty$  without affecting the validity of the equation. Define a new function  $h$  by

$$h(t) = KC(ct/2)R(ct/2) . \quad (3)$$

Then  $V(t)$  can be expressed as

$$V(t) = \int_{-\infty}^{+\infty} P(t-\tau)h(\tau) d\tau , \quad (4)$$

or, using  $*$  to denote the convolution operation,

$$V = P * h . \quad (5)$$

Equations (4) and (5) can be interpreted as saying that  $V(t)$  is the output of a linear system whose input is  $P(t)$  and whose impulse response is  $h(t)$ . Since the problem of determining the aerosol signature is essentially that of determining  $h$ , it may be said that our problem is to deconvolve  $V$  with respect to  $P$ . Other ways of phrasing the problem are (1) determine the impulse response of the system from knowledge of its input and output and (2) determine the input  $h(t)$  that produces a known output  $V(t)$  when the impulse response  $P(t)$  is known. The latter phrasing follows from the fact that  $P * h = h * P$  and is a convenient way of looking at the problem for noise analysis.

## 2.2 Typical Transmitter Pulses, Range Law, and Signatures

The laser probe has undergone several modifications in the course of its history to improve transmitter pulse and receiver noise characteristics. Figure 1 shows the shape of a typical transmitted pulse for the probe's original constitution, measured by using an approximately 100-ps response time photodiode. The measurement was made by intercepting the transmitted pencil beam with the sensitive photodiode surface (an Instrument Technology Ltd. HSD-50) and recording the temporal variation of the induced photocurrent. The peak transmitted power is roughly 5 to 10 W, depending on whether a polarizer is inserted in the beam; the latter is often the case in experimental flight tests because backscatter depolarization effects also are measured. The pulse is about 11 ns wide at the half-maximum points and rises noticeably more rapidly than it falls. The pulse shape needed in equation (4) is, however, the result of filtering that which is shown in figure 1 with the bandpass characteristic of the probe's receiver, which has a bandwidth of approximately 200 MHz. This follows because the signal,  $V(t)$ , is thusly band limited and from the basic algebraic properties of the convolution operation. Little change of pulse shape would occur in figure 1 due to such filtering, though.

The first probe modification resulted in the faster pulse shown in figure 2. The pulse shape was measured by reflecting the transmitter pulse into the probe's receiver system, using a properly oriented flat reflecting surface, and recording the resulting waveform at the receiver output. Thus the pulse shape shown in figure 2, which is about 7 ns FWHM, is that appropriate for use in equation (4). The transmitted optical pulse actually has a much faster leading edge than shown in figure 2. Measurements using the HSD-50 photodiode showed a rise time of about 100 ps, which is the photodiode response time. These measurements and the technical details of the pulser design are discussed by Vanderwall et al.<sup>6</sup> The receiver bandpass of the probe slows this quickly rising pulse to the extent indicated by figure 2.

---

<sup>6</sup>Jonathan Vanderwall, Walter V. Hattery, and Zoltan G. Sztankay, *Subnanosecond Rise Time Injection Laser Pulses*, Harry Diamond Laboratories HDL-TR-1697 (March 1975).

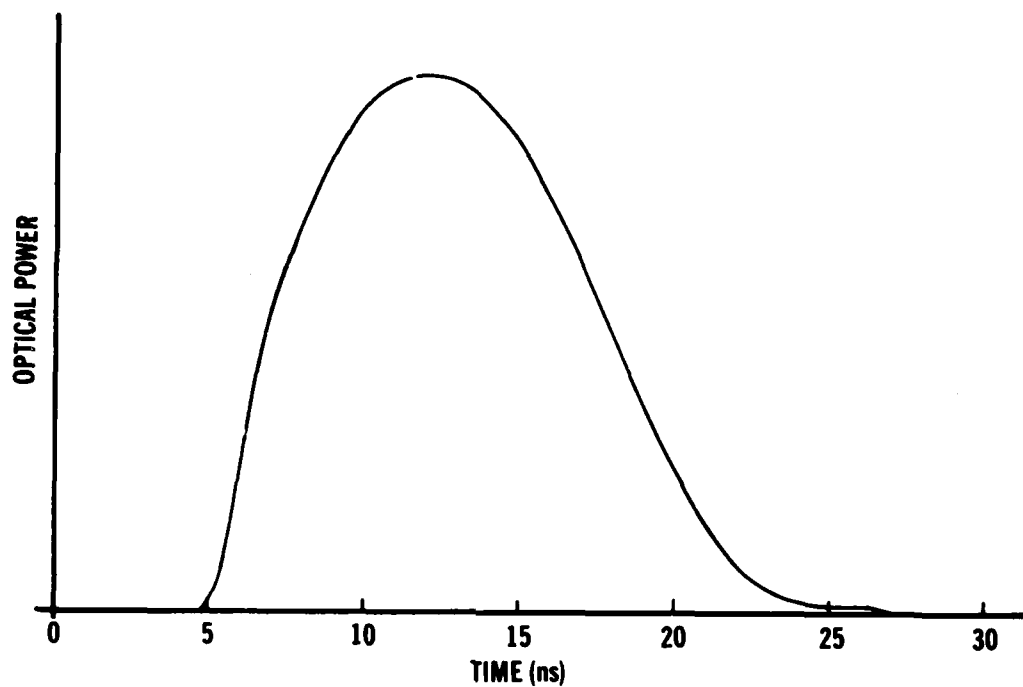


Figure 1. Shape of typical optical pulse from GaAs laser pulser, measured with 100-ps response time photodiode. This pulser was original transmitter section of GaAs laser probe for aerosol backscatter measurements.

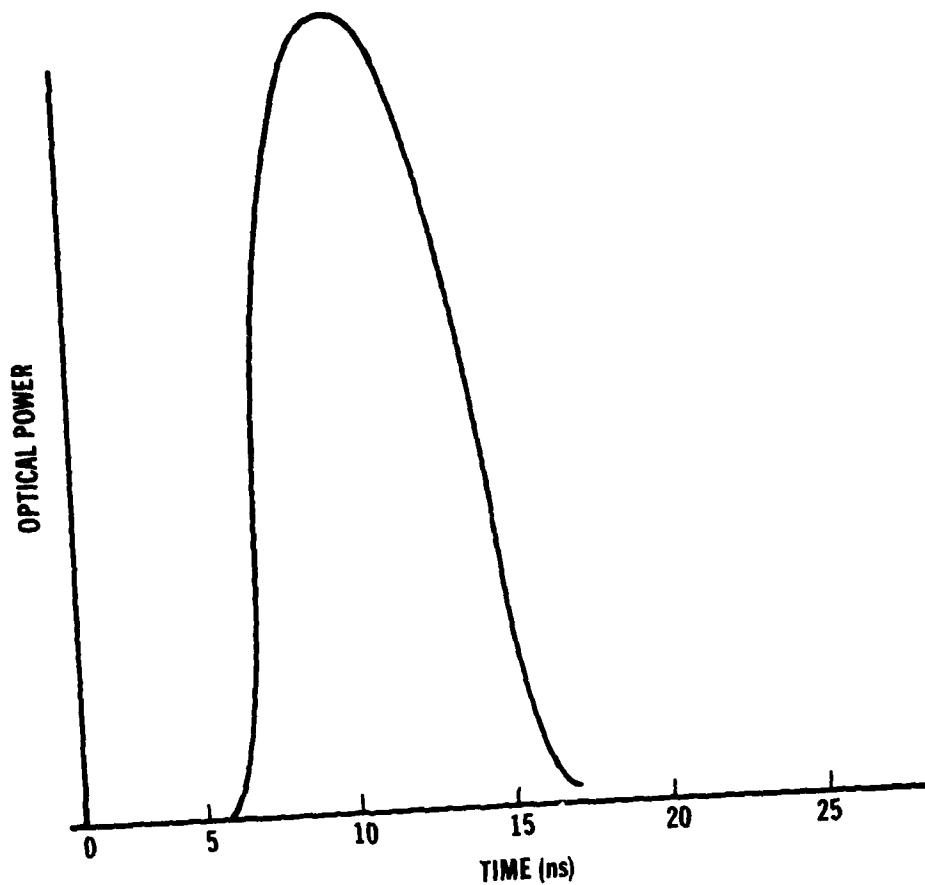


Figure 2. Shape of typical optical pulse from improved GaAs laser pulser. Shape was measured by reflecting transmitted pulse into approximately 200-MHz bandwidth optical receiver essentially collocated with transmitter, by using appropriately oriented flat reflecting surface. This pulser was transmitter section of improved GaAs laser probe for aerosol backscatter measurements.



All backscatter data available at the time of this investigation were obtained with the pulse shapes of figures 1 and 2. Recent modifications have further shortened the transmitter pulses (to about 5 ns FWHM) and have substantially increased the power output level.

The range response of the probe can be adjusted by varying the angle between the transmitter pencil and the receiver field of view and by varying the separation between the transmitter and the receiver. Figure 3 shows a typical range-response curve, one that has been used in several flight tests. Apart from its precise shape, the curve's main adjustable features are the range at which peak response is obtained and the range interval over which the system is sensitive.

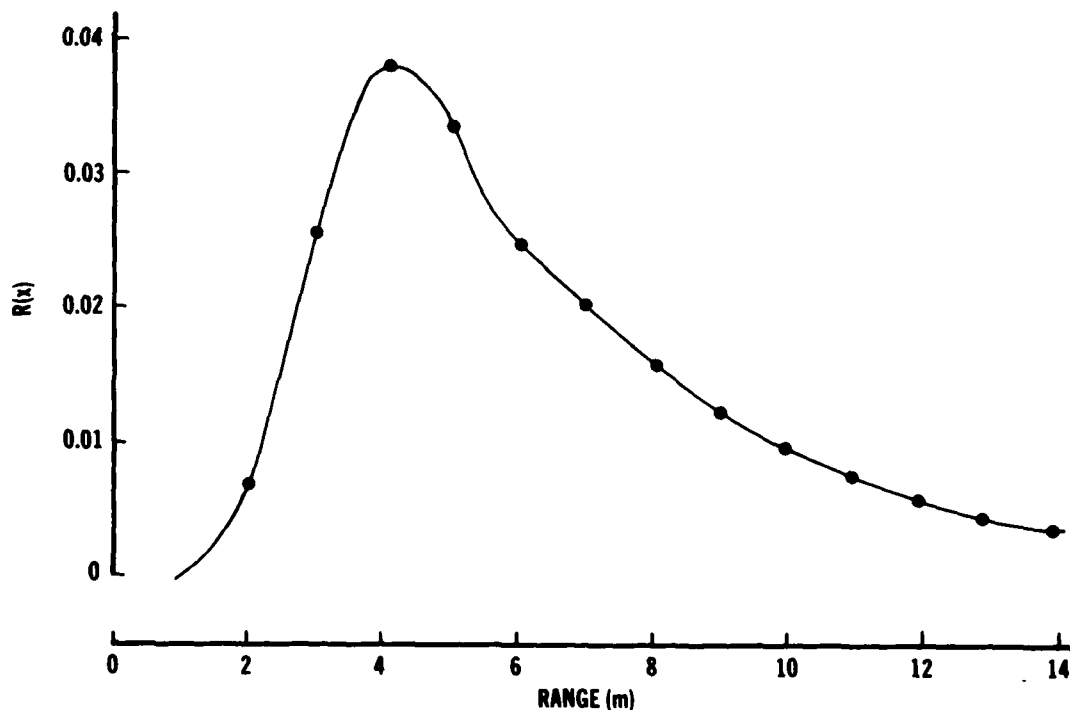


Figure 3. Measured range-response curve,  $R(x)$ , of pencil beam GaAs laser probe for aerosol backscatter measurements. Curve was obtained by measuring peak receiver response to flat reflecting target, oriented at right angles to and filling influence pattern, as function of range from transceiver to target. Circled points indicated measurements. Scale of  $R$  has been normalized so that response at 7 m is  $1/(7 \text{ m})^2$ .

The general features of the aerosol signature,  $C(x)$ , can be determined by considering a somewhat idealized aerosol density profile. Suppose that  $\sigma(x)$  and  $\mu(x)$  are as shown in figure 4. Then  $C$  vanishes for  $x \leq x_0$ . For  $x_0 < x \leq x_1$ ,

$$\int_0^x \sigma(s) ds = (\sigma/l) \int_0^x (s - x_0) ds = (1/2)(\sigma/l)(x - x_0)^2,$$

so that

$$C(x) = (\mu/l)(x - x_0)e^{-(\sigma/l)(x-x_0)^2}. \quad (6)$$

For  $x > x_1$ ,

$$\int_0^x \sigma(s) ds = \int_{x_0}^{x_1} \sigma(s) ds + \int_{x_1}^x \sigma ds = (1/2)(\sigma/l)l^2 + \sigma(x - x_1)$$

so that

$$C(x) = \mu e^{-\sigma l} e^{-2\sigma(x-x_1)} \quad (7)$$

If distances are measured in units of  $l$ , then the three results for  $C(x)$  become

$$\begin{cases} 0, & \text{for } x \leq x_0, \end{cases} \quad (8)$$

$$C(x) = \begin{cases} \mu(x - x_0)e^{-\sigma l(x-x_0)^2}, & \text{for } x_0 < x \leq x_1, \end{cases} \quad (9)$$

$$\begin{cases} \mu e^{-\sigma l} e^{-2\sigma l(x-x_1)}, & \text{for } x > x_1. \end{cases} \quad (10)$$

Thus, with range measured in units of  $l$ , the only parameter upon which  $C(x)/\mu$  depends is  $\sigma l$ . Plots of  $C(x)$  according to equations (8) to (10) for various values of  $\sigma l$  are given in figure 5. The particular value of  $\mu$  determines the vertical scale, and the particular value of  $\sigma$  for a given curve in the figure determines the horizontal scale by determining  $l$ . Put in a more direct way, given the  $\mu$ ,  $\sigma$ , and  $l$  of interest, one chooses the curve corresponding to the product of  $\sigma$  and  $l$ ; then  $\mu$  determines the appropriate vertical scale to use and  $l$  determines the corresponding horizontal scale.

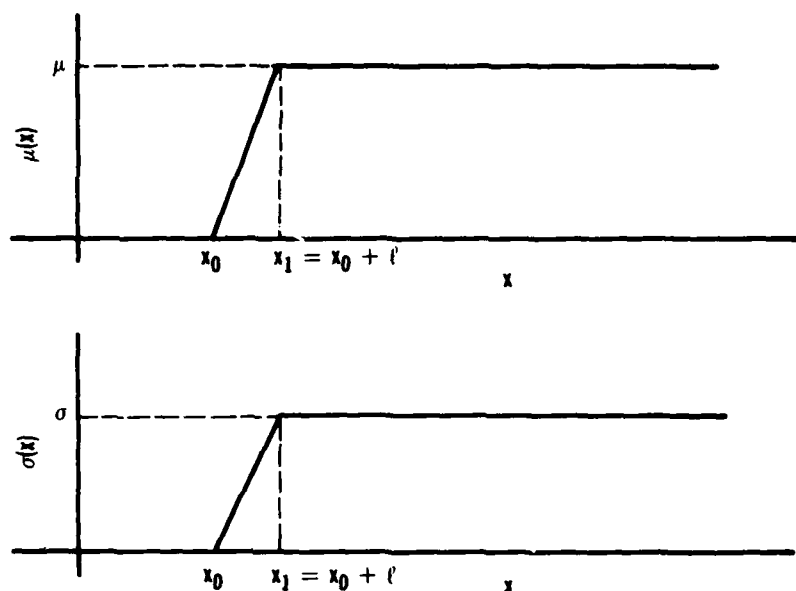


Figure 4. Illustration of idealized aerosol density profile along pencil beam influence pattern of active optical detection system. Profiles of extinction coefficient,  $\sigma$ , and backscatter coefficient,  $\mu$ , are indicated as function of range,  $x$ , from transceiver.

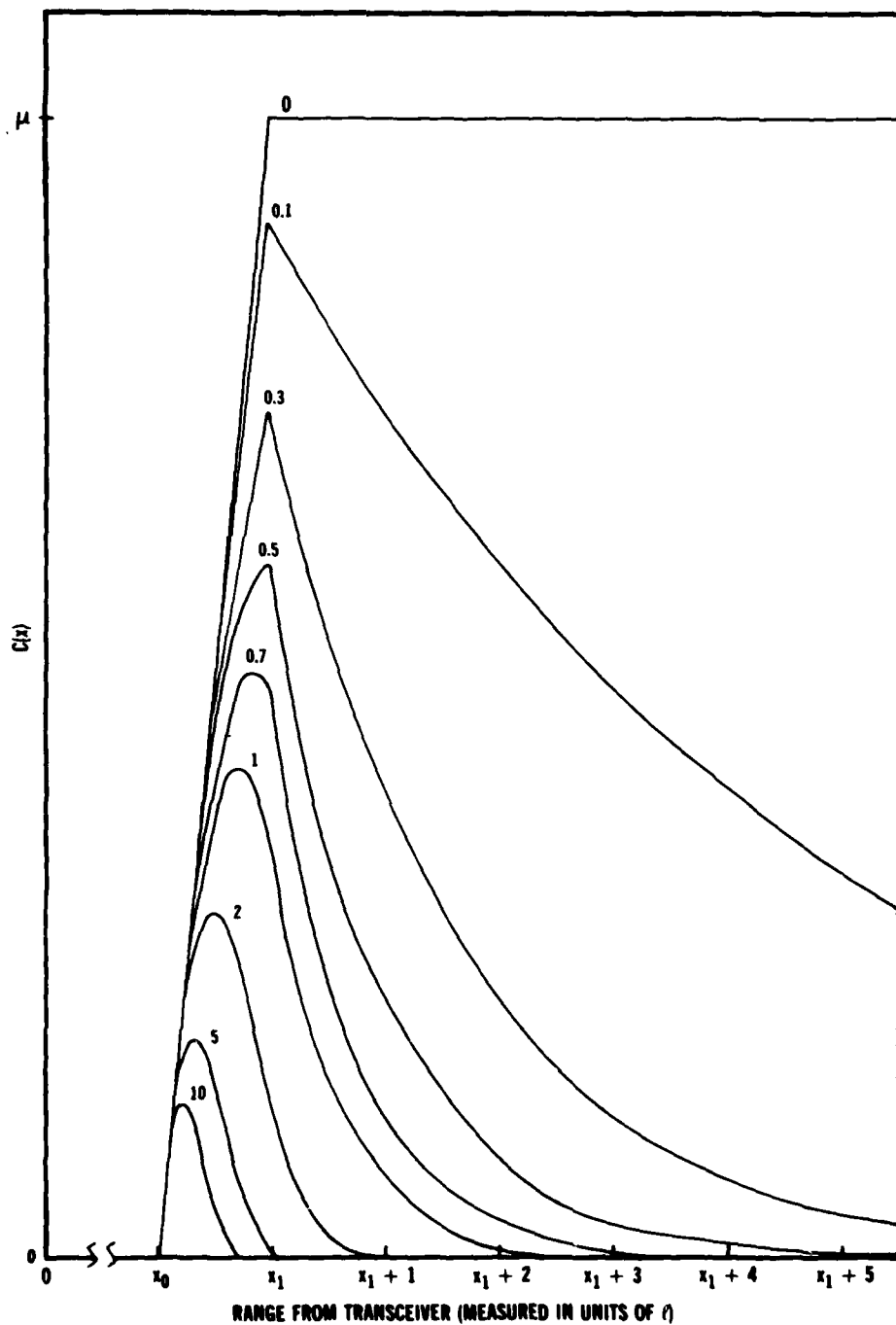


Figure 5. Aerosol signatures,  $C(x)$ , calculated from defining equation (1) for aerosol density profile shown in figure 4 for various values of dimensionless parameter  $\sigma l$  (noted near signature peaks). Range is measured in units of  $l$ , thickness of aerosol buildup region.

Two points should be made about figure 5. First, the corners in the signatures at  $x_0$  and  $x_1$  are due to the corners in the corresponding aerosol density profile. Since the latter never occur in reality, the former are always rounded off in real cases. Second, the mode of presentation is inappropriate for signatures corresponding to the limiting case  $\ell = 0$  because then the entire horizontal scale shrinks to a single point; alternatively, measuring range in units of  $\ell = 0$  is nonsense. For this limiting case, the signature is given by

$$C(x) = \begin{cases} 0, & \text{for } x < x_0 = x_1, \\ \mu e^{-2\sigma(x-x_1)}, & \text{for } x \geq x_1, \end{cases} \quad (11)$$

which is sketched in figure 6.

One further point should be made concerning the aerosol density profile used in the foregoing calculations. The aerosol is assumed to extend infinitely far in the positive range direction, and this extension never occurs in reality. If the range at which the aerosol density begins to drop out is denoted by  $x_2$ , then equations (8) to (10) remain valid, except that in equation (10) the validity is restricted to

$$x_1 < x < x_2.$$

The net effect on the signatures of figure 5 is that, from  $x_2$  to the range where the aerosol finally ceases to exist,  $C(x)$  falls to zero.

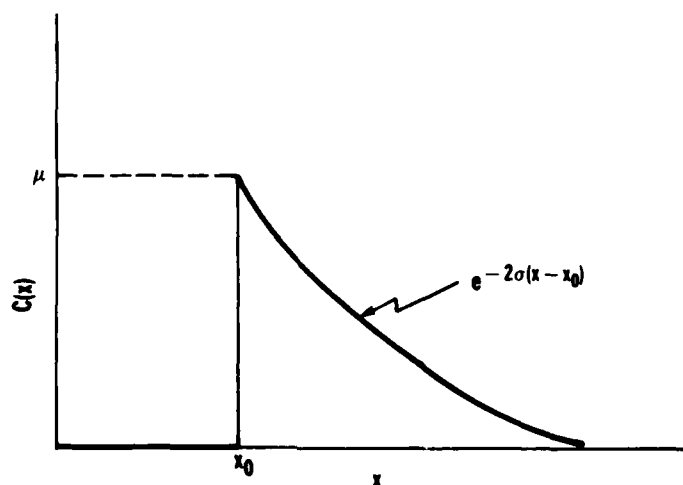


Figure 6. Aerosol signature for semi-infinite uniform aerosol distribution with abrupt buildup at distance  $x_0$  from transceiver.

### 3. FORMAL AND NUMERICAL SOLUTIONS OF DECONVOLUTION PROBLEM

#### 3.1 Formal Solution and Effect of Noise

The deconvolution problem can be solved formally in a straightforward manner, starting from equation (5). The Fourier transform of this equation is

$$\hat{V}(f) = \hat{P}(f)\hat{h}(f) , \quad (13)$$

where  $f$  is the frequency variable and hats are used to denote Fourier transforms. Thus

$$\hat{h}(f) = \hat{V}(f)/\hat{P}(f) , \quad (14)$$

provided that  $\hat{P}(f) \neq 0$ . The time functions  $V(t)$ ,  $P(t)$ , and  $h(t)$  each vanish outside a certain time interval. Their vanishing guarantees the existence and the continuity of their Fourier transforms. If  $f_0$  is a frequency for which  $\hat{P}(f_0) = 0$ , then equation (13) shows that  $\hat{V}(f_0) = 0$  as well. Consequently, the right-hand side of equation (14) takes the indeterminate form  $0/0$  for such frequencies. It is nevertheless true that  $\hat{h}(f_0)$  is well defined, and the continuity of all the transforms involved shows that

$$\hat{h}(f_0) = \lim_{f \rightarrow f_0} \hat{V}(f)/\hat{P}(f) . \quad (15)$$

It is well known that time functions that vanish outside some time interval give rise to Fourier transforms that can vanish at isolated frequencies only. There is therefore no possibility in equation (15) that  $\hat{P}$  will vanish in a neighborhood of  $f_0$ . Thus, if equation (14) is understood to mean the limit in equation (15) at those isolated frequencies where it is singular, the impulse response  $h(t)$  can be obtained from it by using the inverse Fourier transform, namely,

$$h(t) = \int_{-\infty}^{\infty} \left[ \hat{V}(f)/\hat{P}(f) \right] e^{2\pi i f t} df . \quad (16)$$

Equation (16) expresses a formal solution to the deconvolution problem. To implement such a solution numerically involves several difficulties, not the least of which is handling the singular frequencies at which  $\hat{V}$  and  $\hat{P}$  vanish. Any numerical algorithm that

computes the values of  $\hat{V}$  and  $\hat{P}$  from data giving  $V(t)$  and  $P(t)$  potentially commits large errors in determining the ratio  $\hat{V}/\hat{P}$  near singular frequencies. These errors may in turn contribute significant error in the numerical evaluation of the integral in equation (16).

A related difficulty of critical importance pertains to the effect of noise on the signal  $V(t)$  in producing errors in the determination of  $h(t)$ . At singular frequencies of  $\hat{P}$ , the Fourier transform of a noisy signal  $V(t) + n(t)$  is that of the noise, which can only fortuitously turn out to be zero. Near such frequencies, the integrand in equation (16) actually tends to infinity if  $V$  is understood to be that of the noisy signal. Thus, the potential for very large noise related errors in determining  $h(t)$  is clear.

When the noise that accompanies the signal  $V(t)$  is known to be a stationary and Gaussian process, which is a reasonably good assumption for the laser probe,\* a method for analyzing the resulting error present in the determination of  $h(t)$  can be based on the linear system interpretation of equation (5).

The method is suggested by writing equation (5) in the equivalent form

$$V = h * P, \quad (17)$$

which can be interpreted as saying that  $h$  is the input to a linear system with impulse response  $P$  and output  $V$ . Given that the output is accompanied by a well-characterized noise process, the following can be asked: What noise process must accompany the input,  $h$ , in order that the given output noise will be produced, assuming that the system,  $P$ , is internally noiseless? This question can be answered in explicit mathematical terms when the noise processes involved are known to be stationary and Gaussian. Let  $\langle n \rangle$  and  $S_N(f)$  denote the mean and the spectral density of the desired input noise process. Then the mean  $\langle n \rangle$  and the spectral density  $s_n(f)$  of the output noise are given by

$$\begin{aligned} \langle n \rangle &= \langle N \rangle \hat{P}(0), \\ s_n(f) &= |\hat{P}(f)|^2 S_N(f). \end{aligned} \quad (18)$$

---

\*Virtually all the significant noise sources present in direct optical detection systems are of the Johnson or shot-noise type, except possibly the avalanche multiplication noise that arises when avalanche photodiodes are used for detection.

It follows that

$$S_N(f) = s_n(f) / |\hat{P}(f)|^2 \quad (19)$$

for all frequencies such that  $\hat{P}(f) \neq 0$ . The singular frequencies,  $f_0$ , at which  $\hat{P}$  vanishes are isolated; however, they may exist, and unless  $s_n(f)$  tends to zero sufficiently rapidly as  $f \rightarrow f_0$ ,  $S_N(f)$  must become infinite there.

The quantity of interest is actually

$$\int_{-\infty}^{\infty} S_N(f) df ,$$

since this is the mean-squared noise level associated with  $h$ ; denote this quantity by  $\langle N^2 \rangle$ . If  $\langle N^2 \rangle$  can be calculated, it would provide a precise characterization of the error in  $h(t)$  produced by the noise accompanying the signal  $V(t)$ . From this standpoint, infinite singularities in  $S_N(f)$  are acceptable as long as they do not cause the integral giving  $\langle N^2 \rangle$  to diverge.

To progress further with the analysis, some way of dealing with the infinite limits on the integral in question is needed. To see why, note first that both the noise spectrum  $s_n(f)$  and  $\hat{P}(f)$  refer to those that are seen at the receiver amplifier output. In the case of  $\hat{P}(f)$ , the  $P(t)$  from which  $\hat{P}(f)$  is to be determined is the result of filtering the actual transmitted pulse with the receiver bandpass characteristic. Since it is clear that  $\hat{P}(f) \rightarrow 0$  as  $|f| \rightarrow \infty$ , it follows that  $|\hat{P}(f)|^{-2} \rightarrow \infty$  in the same limit. Thus, for the integral in question to converge, it is necessary that  $s_n(f)$  tend to zero sufficiently rapidly as  $|f| \rightarrow \infty$ . Since no measurements of  $s_n(f)$  or  $|\hat{P}(f)|$  are going to reveal the precise analytic behavior of these quantities for large  $|f|$ , recourse to some other procedure that fixes the asymptotic behavior of the integrand is necessary. A reasonable procedure, although certainly not the only one, is to cut off the integration at some frequency,  $f_c$ , that is, to consider only

$$\int_{-f_c}^{f_c} S_N(f) df .$$



This is tantamount to inserting an ideal low-pass filter between the amplifier output and our observation point, which procedure is justifiable if it can be argued that the chosen cutoff frequency introduces negligible distortion in the return pulse from the aerosol.

The foregoing analysis is pursued in section 4, where analytical estimates of the effect of noise are obtained. We now turn to the numerical solution of the deconvolution problem.

### 3.2 Numerical Deconvolution

The inversion of the convolution operator by Fourier transforms, while convenient for analytical purposes, does not lead to the most efficient numerical solution of the problem. To numerically implement such a solution most efficiently would involve the use of the fast Fourier transform. Another approach, which is ideally suited to the digital form of the return pulse data, uses Z-transform techniques. The Z-transform is a discrete counterpart of the Laplace transform and has numerous applications to digital systems and sampled data.<sup>7</sup> To apply Z-transform methods to the deconvolution problem requires first that the problem be cast in discrete form. The method leads to a highly efficient numerical solution.

#### 3.2.1 Discrete Formulation

The transmitted pulse,  $P(t)$ , and the return signal,  $V(t)$ , are observed for  $N$  periodically sampled times,  $\Delta$  seconds apart, in the interval  $[0, \bar{T}]$ , where  $(N - 1)\Delta = \bar{T}$ .<sup>\*</sup> In this case, equation (4) is equivalent to

$$V(t) = \int_0^t P(\tau)h(t-\tau) d\tau, \quad (20)$$

where the commutativity of convolution has been used and it is assumed that  $P(t) = 0$  for  $t < 0$ . For the rest of the formulation, it is necessary to assume also that  $P(0) \neq 0$ ; this restriction may always be achieved by finite time translation. A convenient quantization for  $P$  and  $h$  is

$$P(t) \approx P(n\Delta), \text{ for } n\Delta < t \leq (n + 1)\Delta, \quad (21)$$

<sup>7</sup>E. I. Jury, *Theory and Application of the Z-transform Method*, John Wiley & Sons, Inc., New York (1964).

<sup>\*</sup>The digitization of the data results in  $N = 512$ , with  $\Delta$  typically about 200 ps.

and

$$h(t) \approx h((2n+1)\Delta/2) , \text{ for } n\Delta < t \leq (n+1)\Delta . \quad (22)$$

Evaluation of equation (20) at  $t = n\Delta$  yields

$$V(n\Delta) = \Delta \sum_{i=0}^{n-1} h([(2n-1)\Delta/2] - i\Delta) P(i\Delta) . \quad (23)$$

Equation (23) may be written more compactly in matrix form if the following identifications are made:

$$V' = [V(0), V(\Delta), V(2\Delta), \dots, V((N-1)\Delta)] , \quad (24)$$

$$h' = [h(\Delta/2), h(3\Delta/2), \dots, h((2N-1)\Delta/2)] , \quad (25)$$

and

$$P \approx \begin{bmatrix} P(0) & 0 & 0 & 0 \dots 0 & 0 \\ P(\Delta) & P(0) & 0 & 0 \dots 0 & 0 \\ P(2\Delta) & P(\Delta) & P(0) & 0 \dots 0 & 0 \\ \cdot & \cdot & \cdot & \cdot & \cdot \\ \cdot & \cdot & \cdot & \cdot & \cdot \\ \cdot & \cdot & \cdot & \cdot & \cdot \\ P((N-1)\Delta) & P((N-2)\Delta) & P((N-3)\Delta) & \dots & P(0) \end{bmatrix} , \quad (26)$$

where the prime indicates transposition. Then equation (23) becomes

$$V = \Delta P h . \quad (27)$$

Since  $P(0)$  was assumed nonzero, it follows that the determinant of  $P$  does not vanish so that the matrix  $P$  has a unique inverse  $P^{-1}$ . The solution of equation (27) is therefore

$$h = \frac{1}{\Delta} P^{-1} V . \quad (28)$$

### 3.2.2 Z-Transform Deconvolution

The foregoing discrete formulation shows that the numerical deconvolution problem is essentially to find the inverse of a large matrix or, equivalently, to solve a large number of simultaneous linear equations, namely, equation (27). The Z-transform method can be applied to equation (27) and results in a rather high-speed inversion of  $P$ . To illustrate the results obtainable in this manner, we show in figures 7 to 10 the results of a sample calculation.

Equations (6) and (7) were used with the parameter values  $\sigma = 0.2 \text{ m}^{-1}$ ,  $\mu = 0.01 \text{ m}^{-1} \text{ sr}^{-1}$ ,  $x_0 = 2.75 \text{ m}$ , and  $x_1 = 5.25 \text{ m}$  to compute the aerosol signature shown in figure 7. The parameter values correspond to a potential encounter with a dense water cloud. The equation

$$R(x) = \begin{cases} 0 , & x < 2.67 \text{ m} , \\ 1.83(1 - 2.67/x)(1/x^2) , & 2.67 \text{ m} < x < 5.89 \text{ m} , \\ 1/x^2 , & x > 5.89 \text{ m} , \end{cases} \quad (29)$$

was used to compute the range-response function  $R(x)$ , which fits the measured range-response function of figure 3 with fair to good accuracy. The product of  $R(x)$  and the aerosol signature (which is proportional to  $h$ ) is shown in figure 8. A unit amplitude transmitter pulse,  $u(t)$ , having the form

$$u(t) = \begin{cases} ((1/4)[1 + \cos(vt - \pi)]^2 , & 0 \leq t \leq 2\pi/v , \\ 0 , & \text{otherwise} , \end{cases}$$

was then assumed; the frequency parameter  $\nu$  ( $\approx 471$  MHz) was set by the condition  $c\pi/\nu = 2$  m ( $c\pi/\nu$  is the spatial basewidth of  $u(t)$ ). This model pulse roughly approximates the measured transmitter pulse of figure 2, apart from the origin of the time axis, and was used to calculate the return signal shown in figure 9 from equation (23). In equation (23),  $h$  was taken as given by the CR product of figure 8; that is, the proportionality constant  $K$  was set equal to 1, and  $\Delta$  was set at  $2/3$  ns. Finally, the Z-transform method was used to deconvolve the return signal of figure 9, that is, to solve equation (27) for  $h = CR$ , and the result is shown in figure 10.

The agreement of figures 8 and 10 is excellent, as can be verified by superimposing tracings of the two waveforms. The relative shift in range between the waveforms is not a real discrepancy; the shift is caused by the need for shifting the transmitter pulse in time so that  $P(0) \neq 0$ , a condition required for the deconvolution computations. The agreement obtained shows that noiseless signals can be deconvolved numerically with considerable accuracy. Moreover, the machine calculations needed to produce figure 10 were sufficiently rapid to make the deconvolution of large data banks of aerosol return signals feasible. Unfortunately, the effect of adding even very small amounts of simulated noise to the return signal is catastrophic. To the issues surrounding this fact we now turn.

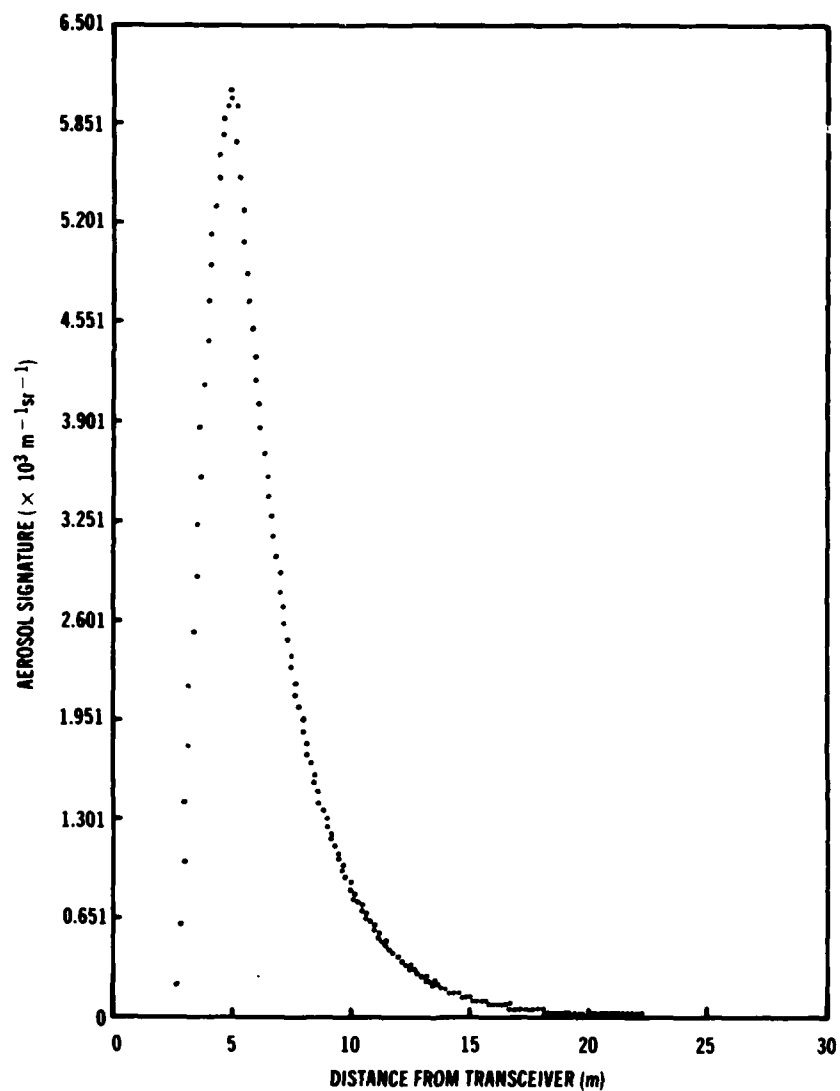


Figure 7. Computed aerosol signature,  $C(x)$ , according to equations (6) and (7) for  $\sigma = 0.2 \text{ m}^{-1}$ ,  $\mu = 0.01 \text{ m}^{-1} \text{ sr}^{-1}$ ,  $x_0 = 2.75 \text{ m}$ , and  $x_1 = 5.25 \text{ m}$ . Parameter values correspond to potential encounter with dense water cloud.

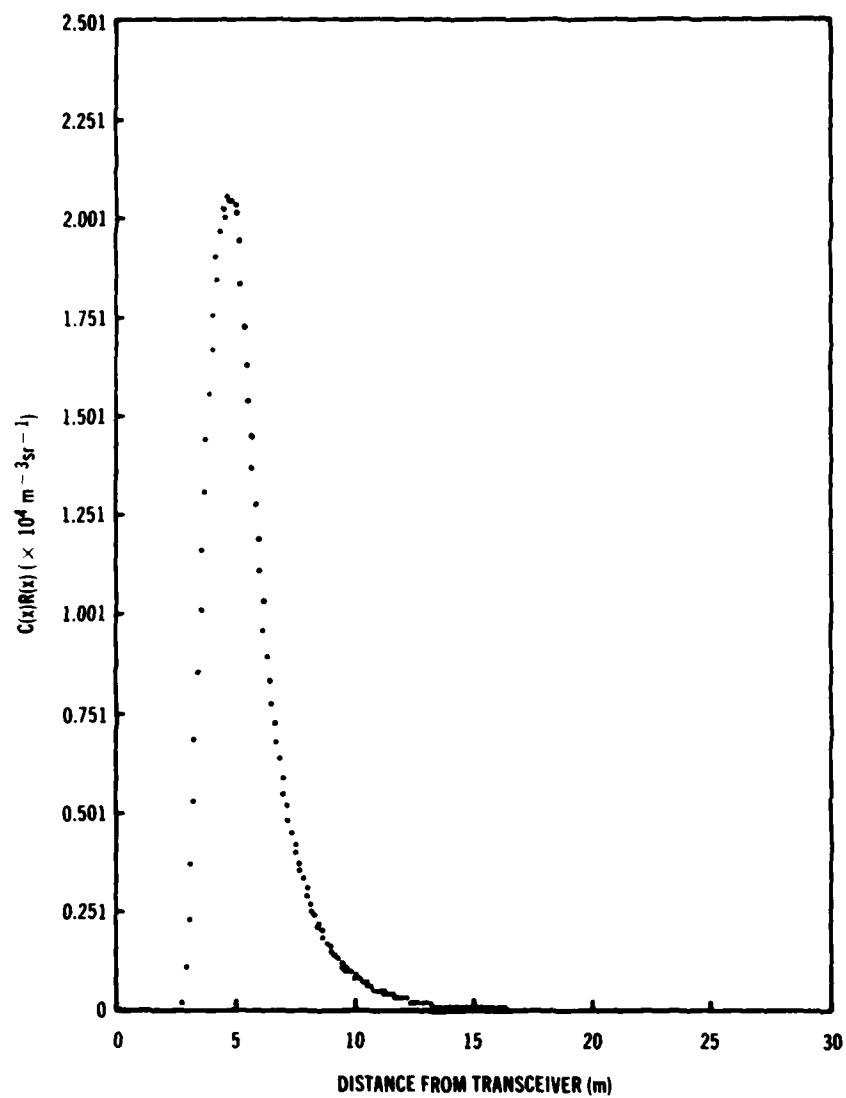


Figure 8. Product of aerosol signature of figure 7 and range-response function,  $R(x)$ , computed from equation (29).

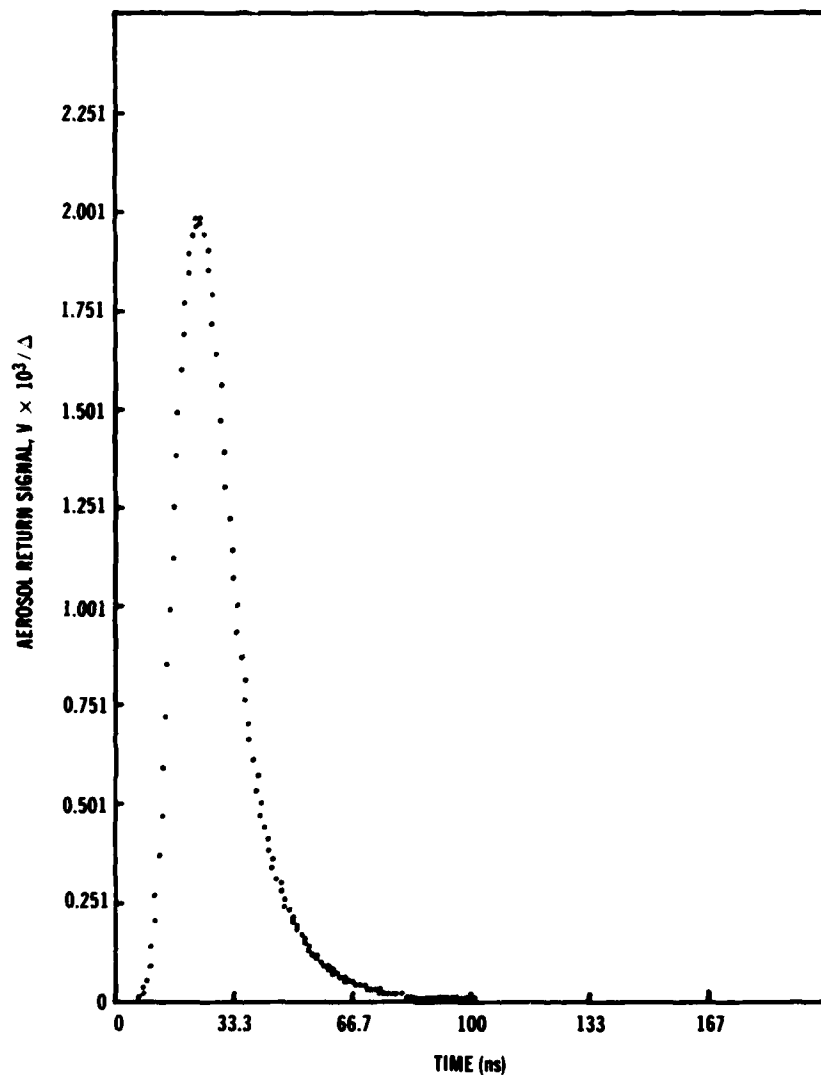


Figure 9. Computed aerosol return signal,  $V$ , according to equation (23) for  $h = CR(K=1)$  as given in figure 8,  $\Delta = 2/3$  ns, and  $P(t) = u(t) = (1/4)[1 + \cos(\nu t - \pi)]^2$  ( $0 \leq t \leq 2\pi/\nu$ );  $\nu$  ( $\approx 471$  MHz) is set by  $c\pi/\nu = 2$  m.

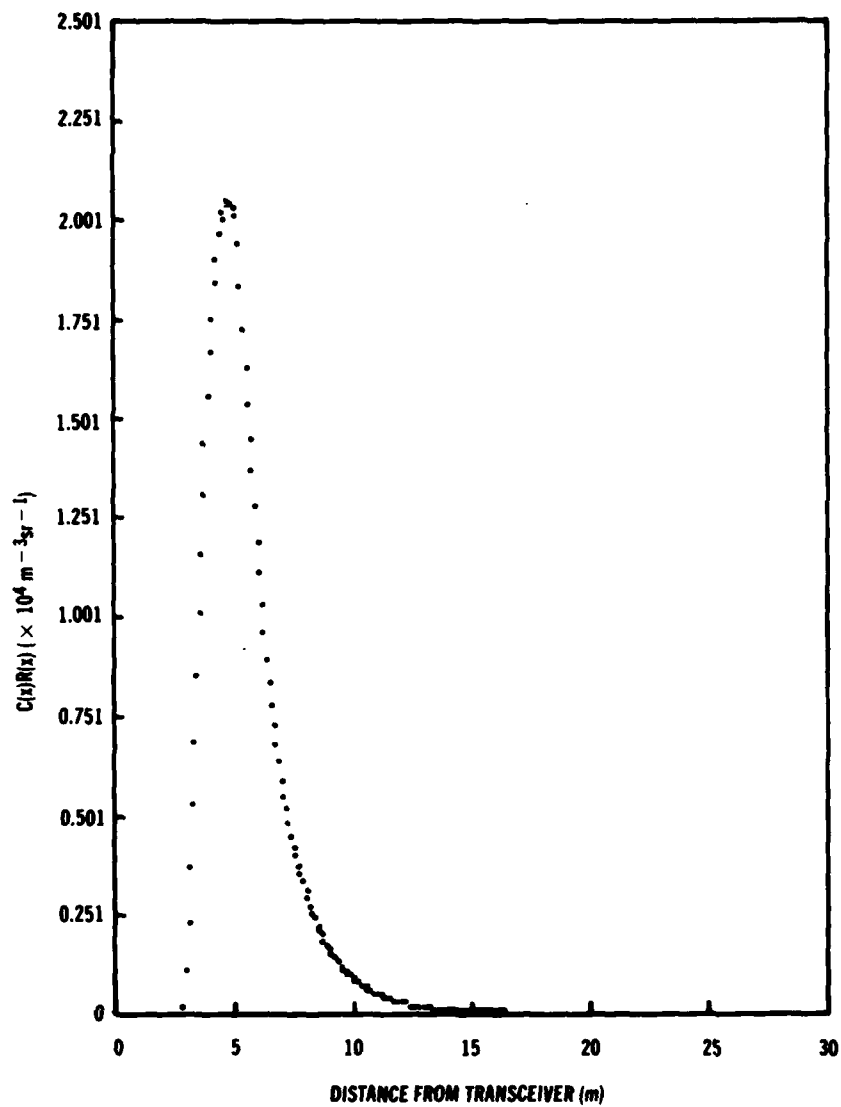


Figure 10. Product of aerosol signature and range response function as determined by Z-transform deconvolution of return signal of figure 9.



#### 4. EFFECT OF NOISE IN SIGNATURE EXTRACTION

##### 4.1 Numerical Effect

In the measurements of aerosol return signals using the GaAs laser probe, various noise sources combine to produce a typical SNR (peak signal divided by rms noise) for all but the most recently obtained data of about 15. To determine the effect of such a noise level on the sample numerical deconvolution just discussed, the return signal of figure 9 was corrupted with simulated noise, giving an overall SNR of 15, and subjected to the Z-transform deconvolution algorithm. The resulting deconvolved signal is shown in figure 11. The effect of the noise was catastrophic. The simulated noise was produced by filtering random numbers with a third-order Butterworth filter with an upper frequency cutoff of 200 MHz (the approximate bandwidth of the amplifiers used in the laser probe's receivers) and then scaling so that the rms value was 1/15 the peak value of the return signal. To determine if the catastrophe would disappear for higher SNR's, the deconvolution computation was repeated for an SNR of 150. The result was similar to that in figure 11.

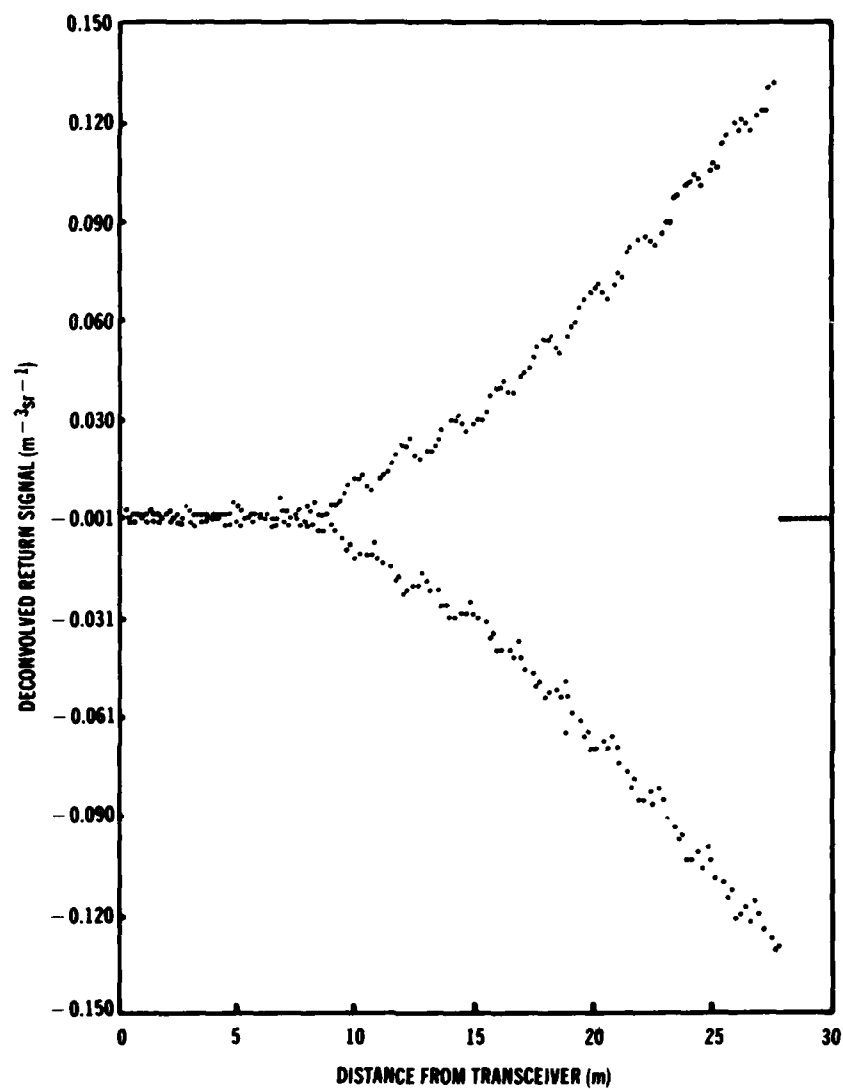


Figure 11. Result of deconvolving return signal of figure 9 after it has been corrupted with simulated noise giving overall signal-to-noise ratio of 15. Noise bandwidth is approximately 200 MHz.

#### 4.2 Analytical Estimation of Noise Effects

This section gives an analysis of the effect of noise by using the ideas and the assumptions of section 3.1. The result of the analysis is that a good understanding of the phenomenon shown by figure 11 is obtained, and the means for overcoming the noise problem are indicated.

The starting point is the equation

$$\langle N^2 \rangle = \int_{-f_c}^{f_c} s_n(f) / |\hat{P}(f)|^2 df \quad (30)$$

for the mean-squared noise level associated with  $h$ ,\* which is proportional to the product of the aerosol signature and the range-response function. Equation (30) follows from the basic relation

$$\langle N^2 \rangle = \int_{-\infty}^{\infty} S_N(f) df, \quad (31)$$

equation (19), and the method chosen to fix the asymptotic behavior of the integrand, namely, to cut off the integral at an unspecified frequency  $f_c$ . Although  $f_c$  is regarded as a variable parameter in what follows, it cannot be chosen too small since it must correspond to enough bandwidth to pass the return signal with good fidelity.

To make an explicit evaluation of equation (30) possible, it is assumed that  $s_n(f)$  is constant over the frequency interval  $-f_c \leq f \leq f_c$  and that the  $P(t)$  from which  $\hat{P}(f)$  is determined is given by the analytical model

$$P(t) = \begin{cases} P_0 \cos^2 (\pi t / 2T), & -T \leq t \leq T, \\ 0, & |t| > T. \end{cases} \quad (32)$$

\*Equation (30) actually gives the mean-squared noise level associated with the result of convolving  $h$  with the impulse response of a filter with sharp lower- and upper-frequency cutoffs at  $-f_c$  and  $f_c$ , respectively.

A plot of the model pulse superimposed on the measured transmitter pulse of figure 2 is given in figure 12.  $P_0$  and  $T$  were chosen to give the model pulse the same peak value and the same FWHM as the measured pulse. The model pulse is only a rough approximation to the measured one primarily because the measured pulse is not symmetric about its peak. The model pulse has the advantage of being easily transformed mathematically in the manner required for the calculation of  $\langle N^2 \rangle$ , however.

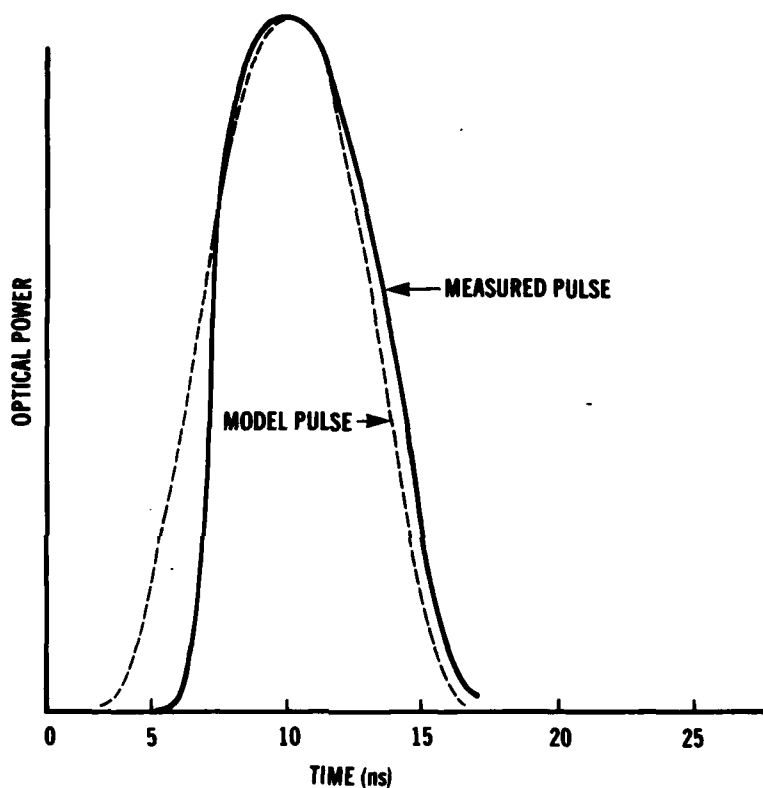


Figure 12. Comparison of shape of model transmitter pulse  $P(t) = P_0 \cos^2 (\pi t/2T)$  with that of measured transmitter pulse of figure 2;  $T$  was chosen to give model pulse same FWHM as measured pulse, and both pulses are aligned to agree at their peaks.

The assumption that  $s_n(f)$  is constant over the frequency interval  $-f_c \leq f \leq f_c$  implies that the mean-squared noise level  $\langle n^2 \rangle$  on the return signal is related to  $s_n$  by

$$s_n = \langle n^2 \rangle / 2f_c ; \quad (33)$$

the return signal being referred to is the actual return signal after being put through an ideal low-pass filter with cutoff frequency  $f_c$ . The Fourier transform of the model transmitter pulse is

$$\hat{P}(f) = \frac{P_o T}{1 - (2fT)^2} \frac{\sin 2\pi fT}{2\pi fT} \quad (34)$$

so that

$$\frac{s_n}{|\hat{P}(f)|^2} = \frac{\langle n^2 \rangle}{2f_c P_o^2 T^2} \left\{ \frac{2\pi fT [1 - (2fT)^2]}{\sin 2\pi fT} \right\}^2. \quad (35)$$

By changing the independent variable to  $x = 2fT$ ,  $\langle N^2 \rangle$  can be written as

$$\langle N^2 \rangle = \frac{\langle n^2 \rangle}{2f_c P_o^2 T^3} \int_0^{2f_c T} \frac{(\pi x)^2 (1 - x^2)^2}{\sin^2 \pi x} dx. \quad (36)$$

Denote the integrand by  $I(x)$  and  $2f_c T$  by  $x_c$ . Then

$$\langle N^2 \rangle = \frac{\langle n^2 \rangle}{2f_c P_o^2 T^3} \int_0^{x_c} I(x) dx. \quad (37)$$

$I(x)$  is everywhere positive and has infinite singularities at  $x = 2, 3, \dots$ ; it is readily verified that, although  $I$  takes the indeterminate form  $0/0$  when  $x = 0$  or  $1$ ,  $I(0) = 1$  and  $I(1) = 4$ . A plot of  $I(x)$  is given in figure 13; the  $x$ -axis has also been labeled with the corresponding frequency variable, assuming that  $T = 7$  ns. It is straightforward to verify that

$$\lim_{x_c \rightarrow 2} \int_0^{x_c} I(x) dx = \infty. \quad (38)$$

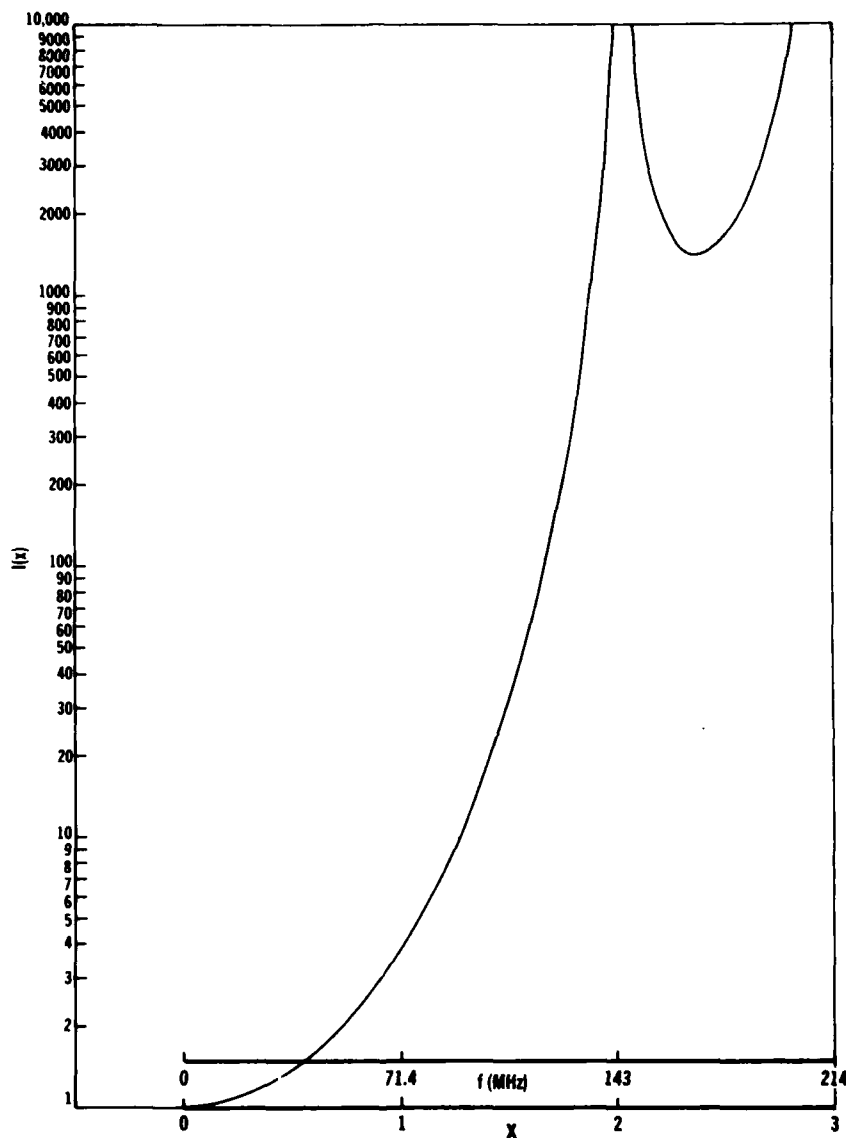


Figure 13. Sketch of graph of  $I(x) = (\pi x)^2 (1 - x^2)^2 / \sin^2 \pi x$ .  
Frequency axis is determined by  $x = 2fT$ , with  $T = 7$  ns.

Consequently, for the model being used, it makes no sense to consider cutoff frequencies beyond  $T^{-1} \approx 143$  MHz. For  $x_c < 2$ , define

$$J(x_c) = \int_0^{x_c} I(x) dx, \quad (39)$$

which is plotted versus  $x_c$  in figure 14. The integral was evaluated numerically by using the trapezoidal rule and an x-axis grid spacing of 0.1. (This approximation slightly overestimates the integral.) Since

$$\langle N^2 \rangle = (s_n / P_o^2 T^3) J(x_c) \quad (40)$$

(eq. 33 has been used here), the curve of figure 14 shows the variation of  $\langle N^2 \rangle$  with the cutoff frequency.

The mathematical origin of the divergent behavior of  $\langle N^2 \rangle$  as  $f_c \rightarrow T^{-1}$  is the vanishing of  $\hat{P}(f)$  as  $f \rightarrow T^{-1}$ . Any transmitter pulse whose Fourier transform has real zeros will cause the type of divergence indicated in figure 14. This fact can be seen as follows. Let  $\bar{f}$  denote the smallest positive zero of  $\hat{P}(f)$ . Since  $\hat{P}(f)$  is an even function, it follows that

$$\langle N^2 \rangle = 2 \int_0^{f_c} s_n(f) / |\hat{P}(f)|^2 df \equiv g(f_c). \quad (41)$$

Since  $\hat{P}(f)$  is necessarily an analytic function for all  $f$ , it has the Taylor expansion

$$\hat{P}(f) = \left. \frac{d\hat{P}}{df} \right|_{f=\bar{f}} (f - \bar{f}) + \frac{1}{2} \left. \frac{d^2\hat{P}}{df^2} \right|_{f=\bar{f}} (f - \bar{f})^2 + \dots, \quad (42)$$

which converges for all  $f$ . In a sufficiently small neighborhood of  $\bar{f}$ ,  $\hat{P}(f)$  can be uniformly approximated by an expression of the form  $a(f - \bar{f})^m$ , where "a" is a nonzero constant and  $m \geq 1$  is an integer. Thus if  $s_n(f)$  is merely finite and nonzero in a neighborhood of  $\bar{f}$ , it follows that

$$\lim_{f_c \rightarrow \bar{f}} g(f_c) = \infty. \quad (43)$$

Equations (41) and (43) show that  $\langle N^2 \rangle \rightarrow \infty$  as  $f_c \rightarrow \bar{f}$ .

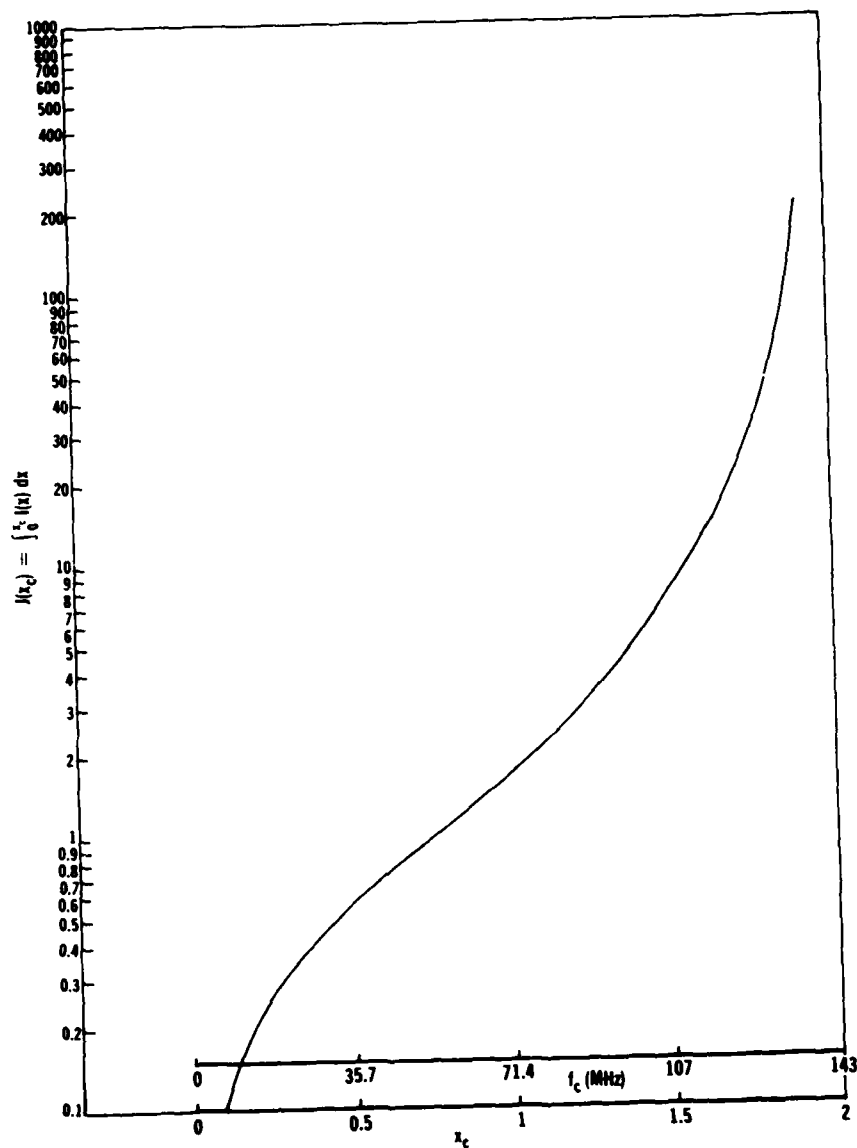


Figure 14. Sketch of graph of  $J(x_c) = \int_0^{x_c} I(x) dx$  versus  $x_c$  and versus  $f_c = x_c/2T$ , with  $T = 7$  ns.



The measured transmitter pulse shown in figure 2 has been numerically Fourier transformed for frequencies up to 250 MHz, and the transform has been found to have no zeros in this range. Consequently, the divergence problem will not occur for this transmitter pulse.

It can be argued that the model being used is approximately correct for all values of  $f_c < T^{-1}$ . The validity of the model with a restricted range for  $f_c$  can be seen by considering the problem in a broader perspective. Let  $h_\ell$  denote the impulse response of an arbitrary low-pass filter. The mean-squared noise level accompanying  $h * h_\ell$  is given by an expression similar to that of equation (30), namely,

$$\int_{-\infty}^{\infty} \frac{s_n(f)}{|\hat{P}(f)|^2} |\hat{h}_\ell(f)|^2 df.$$

This result follows by applying the arguments surrounding equations (17) to (19) to the equation  $V * h_\ell = (h * h_\ell) * P$  and then noting that the spectral density of the noise accompanying  $V * h_\ell$  is given in terms of that for  $V$  by  $|\hat{h}_\ell(f)|^2 s_n(f)$ . By choosing an ideal low-pass filter with a sharp cutoff at  $f_c$ , we effectively took

$$h_\ell(t) = 2f_c (\sin 2\pi f_c t) / 2\pi f_c t \equiv h_c(t) \quad (44)$$

since  $|\hat{h}_c(f)|^2 = 1$  for  $|f| \leq f_c$  and vanishes otherwise. For the general filter, the basic requirement for the analysis is that the integral expression preceding equation (44) be finite. Divergence can come from two sources: the infinite limits on the integral and any zeros of  $\hat{P}(f)$ . The infinite limits are handled by choosing filters with appropriate asymptotic behavior as  $f \rightarrow \pm\infty$ , such as those with sharp cutoffs. The zeros of  $\hat{P}(f)$  can be handled only by choosing filters such that  $\hat{h}_\ell$  vanishes sufficiently fast at the zeros to overcome the divergence that is automatically present in equation (41) as  $f_c$  tends to a zero of  $\hat{P}(f)$ . Therefore, the basic requirement for the ideal low-pass filter with sharp cutoff frequency  $f_c$  is that  $f_c$  be less than the smallest positive zero of  $\hat{P}(f)$ . The last point is important for understanding the behavior shown in figure 11.

We now proceed with the analysis for the model transmitter pulse, keeping the points just raised in mind.

Let  $h_m'$  denote the maximum value of  $h * h_c$ . Then according to equation (40), the SNR necessarily connected with the determination of  $h * h_c$  is

$$(\text{SNR})_{h \cdot h_c} = h_m^2 P_o T^3 / [s_n J(x_c)]^{1/2} . \quad (45)$$

The SNR associated with  $V \cdot h_c$  is

$$\begin{aligned} (\text{SNR})_{V \cdot h_c} &= V_m^2 / (\langle n^2 \rangle)^{1/2} \\ &= V_m^2 / (2 f_c s_n)^{1/2} , \end{aligned} \quad (46)$$

where  $V_m$  is the peak value of  $V \cdot h_c$ . Since the transmitter pulse has very short duration, a large error will not result from using the approximate relationship  $V_m^2 \approx E h_m^2$ , where  $E = P_o T$  is the total energy in the transmitted optical pulse described by equation (32). Equations (45) and (46) then combine to yield

$$(\text{SNR})_{h \cdot h_c} \approx [x_c / J(x_c)]^{1/2} (\text{SNR})_{V \cdot h_c} . \quad (47)$$

If the SNR's of  $V$  and  $V \cdot h_c$  are compared, one finds approximately that

$$(\text{SNR})_{V \cdot h_c} \approx (f_a / f_c)^{1/2} (\text{SNR})_V , \quad (48)$$

where  $f_a$  is the receiver amplifier bandwidth. Combining equations (47) and (48) results in

$$(\text{SNR})_{h \cdot h_c} \approx [x_c / J(x_c)]^{1/2} (f_a / f_c)^{1/2} (\text{SNR})_V , \quad (49)$$

which is the main result of the analysis.

Equation (49) indicates how, depending on the chosen cutoff frequency, noise errors in the return signal  $V$  are translated into noise errors in  $h \cdot h_c$ . The factor  $[x_c / J(x_c)]^{1/2}$  versus  $x_c$  is plotted in figure 15. It shows the progressive degradation in  $(\text{SNR})_{h \cdot h_c}$  compared with  $(\text{SNR})_{V \cdot h_c}$  as the cutoff frequency increases toward  $\approx 143$  MHz, where  $(\text{SNR})_{h \cdot h_c}$  vanishes. The situation improves significantly if the measured transmitter pulse of figure 2 is used for the analysis. Figure 16 plots the SNR penalty factor of this case, namely,  $(\text{SNR})_{h \cdot h_c} / (\text{SNR})_{V \cdot h_c}$ . Also included in the figure is a segment of the

curve of figure 15 for comparison. The SNR penalty factor curve for the measured transmitter pulse was obtained from the numerically determined Fourier transform of the pulse in figure 2 by evaluating the formula

$$\text{SNR penalty factor} = \left[ \frac{f_c}{|\hat{P}(0)|^2 \int_0^{f_c} \frac{df}{|\hat{P}(f)|^2}} \right]^{1/2} \quad (50)$$

numerically for various values of  $f_c$ .

If  $f_c \approx f_a \approx 200$  MHz, figure 16 indicates that

$$(\text{SNR})_{h \cdot h_c} \approx 0.15(\text{SNR})_v.$$

Thus for the 15-to-1 SNR typical of much of the aerosol return signal data, the SNR of  $h \cdot h_c$  is predicted to be about 2. If the aerosol return signal had an SNR 10 times this typical value, the SNR of  $h \cdot h_c$  would be about 20. These predictions apparently contradict the results of figure 11 and the corresponding results for a simulated return signal with a 150-to-1 SNR. There are important differences between the transmitter pulses for the two cases, however.

The results of figure 11 were obtained for a transmitter pulse,  $P_{11}$ , given by

$$P_{11}(t) = \begin{cases} (P_0/4)(1 + \cos vt)^2, & |t| \leq \pi/v, \\ 0, & |t| > \pi/v, \end{cases} \quad (51)$$

where  $P_0$  is the peak transmitted power and  $v \approx 471$  MHz. By a somewhat tedious calculation, the Fourier transform of  $P_{11}$  can be found to be

$$\hat{P}_{11}(f) = 3P_0 \frac{\pi}{v} \frac{\sin \pi x}{\pi x} \frac{1}{(4 - x^2)(1 - x^2)}, \quad (52)$$

where  $x = 2\pi f/v$ . The expression for  $\hat{P}_{11}$  has an infinite number of zeros, namely, for  $f = \pm 3v/2\pi, \pm 4v/2\pi, \dots$ . The smallest positive zero is  $f = 3v/2\pi \approx 225$  MHz.

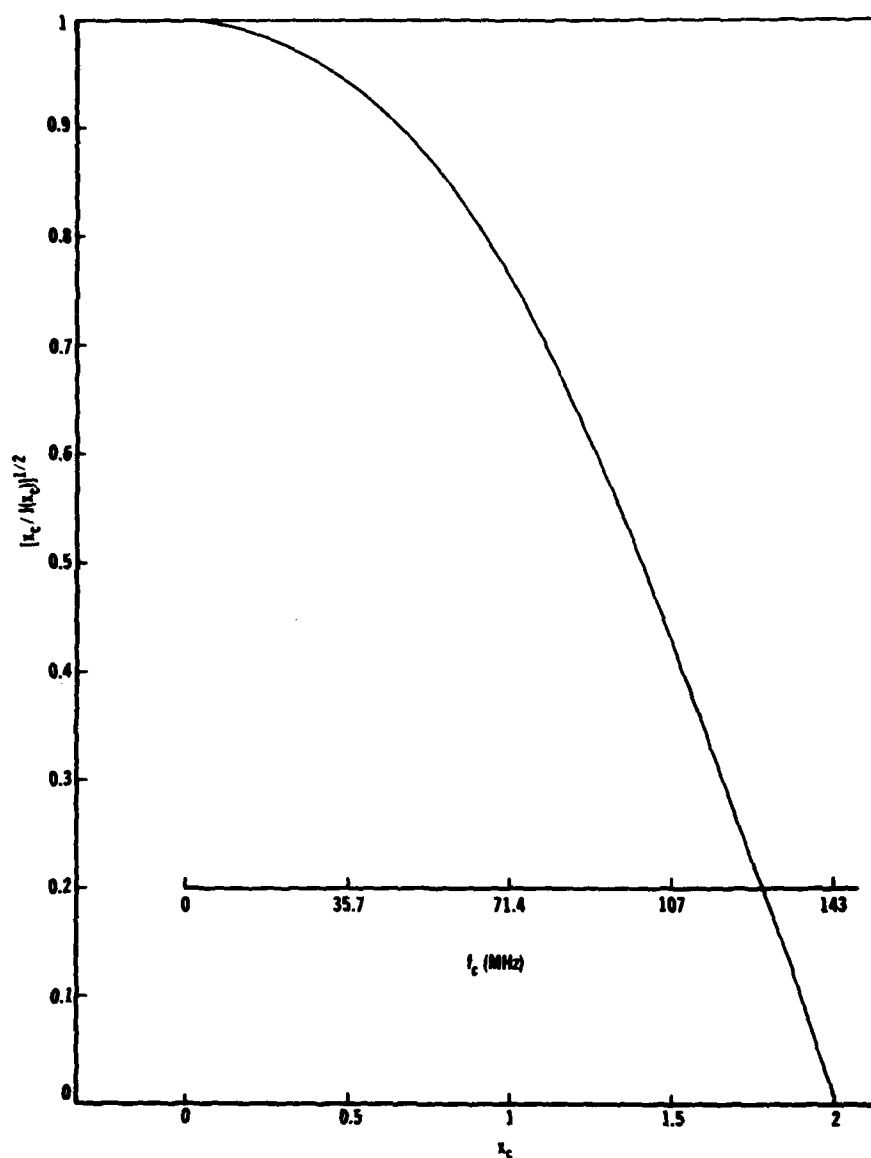


Figure 15. Signal-to-noise-ratio penalty factor  $[x_c/J(x_c)]^{1/2}$  versus  $x_c$  and  $f_c$  for model transmitter pulse of equation (32).  $J(x_c)$  is defined by equation (39) and figure 13,  $x_c = 2f_c T$ , and  $T = 7$  ns for  $f_c$  axis labeling.

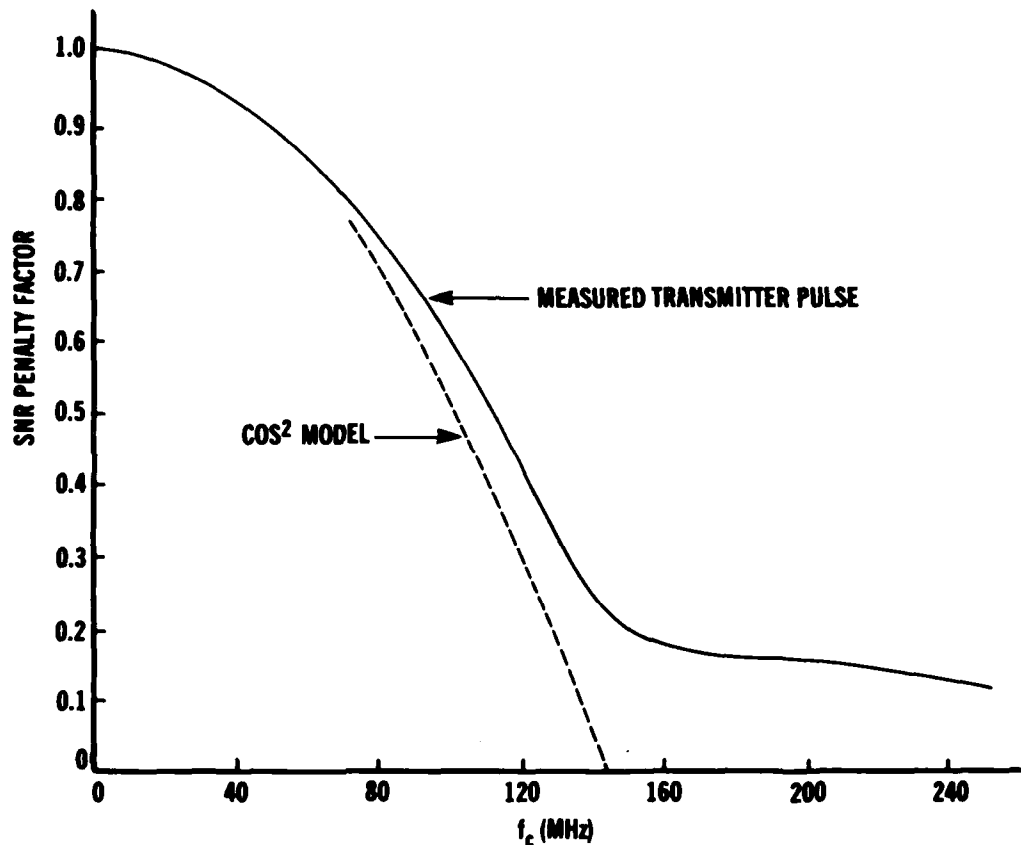


Figure 16. Signal-to-noise ratio penalty factor versus  $f_c$  for measured transmitter pulse of figure 2 and segment of signal-to-noise ratio penalty factor curve of figure 15 for comparison.

The Butterworth filter used to establish the frequency band for the simulated noise that produced the results of figure 11 does not have a vanishing frequency response at 225 MHz. Therefore, in accordance with previous discussion, divergent behavior in the noise accompanying the deconvolved signal is expected, regardless of the SNR of the aerosol return signal.

The unacceptably low SNR of  $h * h_c$  ( $\approx 2$ ) predicted with equation (50) for  $f_c = 200$  MHz and a measurement SNR of 15 to 1 can be improved by lowering  $f_c$ . This tack does not lead to acceptable results, however, because reasonably good SNR's are obtained only for values of  $f_c$  that significantly affect the shape of the return pulses. The simple signature extraction procedure of assuming that the transmitted pulse is

approximately a temporal  $\delta$ -function gives an approximation of  $h$  that is smeared by a roughly 2-m averaging of the desired impulse response. This approximation is corrupted also by the measurement noise, but the SNR is the same for  $h$  as for the measured signal  $V$ . Thus the simple procedure and the full deconvolution procedure with its parameter  $f_c$  can be compared as follows. The former gives an SNR equal to that of the return pulse data and a signature shape distorted by a roughly 2-m averaging. In the latter, both the SNR and the signature shape distortion depend on  $f_c$  in the manner of a tradeoff, and there is no advantage in using the more complex procedure if an improvement of the 2-m averaging and an acceptable SNR cannot be obtained with it. Our results show that such improvement and an acceptable SNR cannot be obtained for the 15-to-1 measurement SNR typical of much of the back-scatter data. Nonetheless, a sufficiently high measurement SNR, which may now be available due to recent probe modifications, would change this conclusion.

Several additional approaches could be pursued to improve signature extraction accuracy. One could attempt to modify the transmitter pulse shape so as to improve the SNR penalty characteristic. One could also replace the sharply cutoff observation filter with a more general type and seek to optimize the results as a function of the filter characteristic. Certainly the most direct approach is to further increase the peak transmitted power so as to improve the measurement SNR. Finally, the use of a priori knowledge about  $C(x)$  together with parameter estimation techniques could be pursued. The latter approach, which constitutes a new strategy, is given a preliminary discussion in the next section.

## 5. ALTERNATIVE APPROACH THROUGH PARAMETER ESTIMATION

The problem whose discussion has occupied the bulk of this report is an example of what is known mathematically as an ill-posed problem, that is, one whose solution does not depend continuously on the given data. For such problems, there is no guarantee that reduction of the errors in the given data will reduce the error in the solution, and this lack of guarantee would seem to indicate that the practical obtainment of solutions to ill-posed problems is a matter of fortuity. Such a conclusion is false, however, because solution methodology is available. Ill-posed problems are currently of considerable interest in a number of application areas, particularly in the geophysical interpretation of seismic data. The general approaches to a practical solution include the selective reduction of the information sought and the use of any a priori knowledge concerning the object under study to provide further con-

straints on the problem. Our use of a low-pass observation filter is an example of the selective information-reduction strategy. This section of the report discusses a preliminary investigation of applying a priori knowledge together with the use of parameter estimation techniques as an alternative approach.

The main source of a priori knowledge for the signature extraction problem is contained in equation (1), which defines the signature in terms of the physical properties  $\sigma$  and  $\mu$  of the aerosol. Let us model the aerosol distribution in the influence pattern of the GaAs probe as a sequence of layers of nonzero thickness, within each of which the physical parameters  $\sigma$  and  $\mu$  are constant, but allowing that the parameter values in each of the layers be arbitrary. This distribution of parameter values will be the problem solution that we propose to determine from measured aerosol return signals. How can this determination be made?

Suppose that the aerosol distribution model has  $M$  layers, so that the  $2M$  parameters  $\sigma_1, \mu_1, \sigma_2, \mu_2, \dots, \sigma_M, \mu_M$ , which we denote vectorially by  $\underline{g}, \underline{\mu}$ , are sought. By using equation (1) and the model, the corresponding aerosol signature  $C(x, \underline{g}, \underline{\mu})$  can be calculated analytically and depends on our  $2M$  parameters. By next using equation (2), a similarly parameterized return signal  $V(t, \underline{g}, \underline{\mu})$  can be calculated. The final step is to seek the parameter values that minimize, in some sense, the difference between  $V(t, \underline{g}, \underline{\mu})$  and the measured return signal.

There is no question concerning the existence of solutions to the type of minimization problem outlined since the dependence of  $V(t, \underline{g}, \underline{\mu})$  on  $\underline{g}$  and  $\underline{\mu}$  is continuous, and attention can be restricted to a compact region of the  $2M$ -dimensional parameter space in seeking solutions (because a priori we know reasonable bounds on the physical parameters). Difficulties could arise, however, if several relative minima are present, or in implementing a numerical solution for fairly large values of  $M$ .

The approach just outlined makes substantial use of a priori information about  $C(x)$  and, if successful, will yield a mathematical formula for a continuous solution to the signature extraction problem. Moreover, the method will actually give approximate extinction and backscatter coefficient profiles (along the influence pattern) so that more information than is contained in the aerosol signature may be obtained. The validity of the solution will, of course, be limited by the noise accompanying the measured signal, but this limitation is no worse than the measurement noise. The potential lack of uniqueness of the solutions could pose a more serious problem if all but one of them could not be ruled out on a priori grounds.

### 5.1 Estimation of $\sigma$ and $\mu$ for Uniform Aerosol

To test the utility of the foregoing approach, the following problem was considered. Suppose that the GaAs probe is fully immersed in a uniform density aerosol with constant values of  $\sigma$  and  $\mu$  throughout. Then

$$C(x) = \mu e^{-2\sigma x} . \quad (53)$$

If a measured return signal is known to have been obtained under such circumstances, then the problem of determining the values of  $\sigma$  and  $\mu$  from the measured signal can be posed. This is the simplest conceivable problem of the type being considered. We discuss its solution in the discrete framework of section 3.2.1.

We assume that the transmitted pulse and the measured return signal are observed for  $N$  periodically sampled times,  $\Delta$  seconds apart, in the interval  $[0, T]$ , where  $T = (N - 1)\Delta$ . The quantization chosen by equation (21) gives rise to the  $N \times N$  matrix  $P$  of equation (26), while equation (24) gives the corresponding discrete representation of the measured return signal. Equation (24) defines an  $N$ -component row vector  $V'$  so that the corresponding column vector is denoted by  $V$ . Let  $h(\sigma, \mu)$  denote the column vector with components  $\mu e^{-\sigma c n \Delta} R(c n \Delta / 2)$ ,  $n = 0, 1, \dots, N - 1$ . Then the column vector representation of our parameterized return signal  $V(t, \sigma, \mu)$  is  $\Delta Ph(\sigma, \mu)$ . Thus we seek to minimize, in some sense, the vector  $\Delta Ph(\sigma, \mu) - V$ .

The minimization problem is considered for a general quadratic cost function

$$J(\sigma, \mu) = (\Delta Ph(\sigma, \mu) - V)' A (\Delta Ph(\sigma, \mu) - V) , \quad (54)$$

where  $A$  is any fixed positive definite  $N \times N$  matrix; the prime notation indicates the transpose operation. The problem is to find specific values  $\bar{\sigma}$  and  $\bar{\mu}$  for  $\sigma$  and  $\mu$  that minimize  $J$ . If  $A$  is the identity matrix, then the minimization is in the least-squares sense; taking  $A$  as other than the identity matrix allows for various other weightings of the difference vector  $\Delta Ph(\sigma, \mu) - V$ . A standard approach for such minimization problems is the method of steepest descent--a method of iteratively refining estimates of  $\bar{\sigma}$  and  $\bar{\mu}$  by adjusting their values dependent upon the behavior of the gradient of the cost function.<sup>8</sup>

<sup>8</sup>A. Sage and J. Melsa, *System Identification*, Academic Press, Inc., New York (1971).



The method revolves critically on one's ability to determine a sequence  $\{k_i\}$  of constants with certain convergence-insuring properties. Specifically, let  $\sigma_i$  and  $\mu_i$  denote the estimates at the  $i$ th stage of the descent, and let  $J_i = J(\sigma_i, \mu_i)$ . For  $\sigma_{i+1}$  and  $\mu_{i+1}$ , we take

$$\begin{pmatrix} \sigma_{i+1} \\ \mu_{i+1} \end{pmatrix} = \begin{pmatrix} \sigma_i \\ \mu_i \end{pmatrix} - k_i \begin{pmatrix} \frac{\partial J}{\partial \sigma} \big|_{\sigma_i, \mu_i} \\ \frac{\partial J}{\partial \mu} \big|_{\sigma_i, \mu_i} \end{pmatrix} \quad (55)$$

where the  $k_i$  must be such that  $J_i \geq J_{i+1}$  at every stage of the descent, and equality holds only in the case  $J_i = J_{i+1} = 0$ . The explicit construction of  $\{k_i\}$  for a given problem can be very difficult so that such sequences are often established by empirical investigation. Such investigation was the tack chosen for the problem at hand.

Figure 17 shows the constant-cost contours of  $J$  for  $A =$  the identity matrix and for the true values  $\sigma = 0.2 \text{ m}^{-1}$  and  $\mu = 0.01 \text{ m}^{-1} \text{ sr}^{-1}$ . Qualitatively similar pictures are obtained for other true values of  $\sigma$  and  $\mu$ . Since the family of trajectories orthogonal to the constant-cost contours gives the directions of the vector gradient of  $J$ , the examination of such pictures can suggest appropriate paths for the descent and point out potential difficulties.

The steepest-descent algorithm for  $k_i = 1/i$  was implemented on a computer for the problem with true values  $\sigma = 0.2 \text{ m}^{-1}$  and  $\mu = 0.01 \text{ m}^{-1} \text{ sr}^{-1}$ . Trajectories using different initial step sizes (to establish the first gradient computations) and 25 iterations for  $\sigma$  and  $\mu$  are shown in figure 18. A choice for the matrix  $A$  that weighted the values of the return signal more heavily near its peak produced similar results.

In addition to steepest descent, an intuitive algorithm for estimating  $\sigma$  and  $\mu$  was investigated. The algorithm is based on the observation that the peak of the return signal depends more strongly on  $\mu$ , while the decay of the trailing edge depends more strongly on  $\sigma$ . Accordingly, the following algorithm was implemented on a computer:

- a. If the peak signal value is smaller than the peak value of  $\Delta \text{Ph}(\sigma, \mu)$ , then decrease  $\mu$ ; otherwise, increase  $\mu$ .
- b. If the trailing edge of the signal, on the average, decays more rapidly than that of  $\Delta \text{Ph}(\sigma, \mu)$ , then increase  $\sigma$ ; otherwise, decrease  $\sigma$ .

The sequence  $\{1/i\}$  was used again to scale each iteration. The results obtained with this algorithm are shown for several typical computations in figure 19, which plots trajectories for several different step sizes and for the same true values of  $\sigma$  and  $\mu$  used in the foregoing examples.

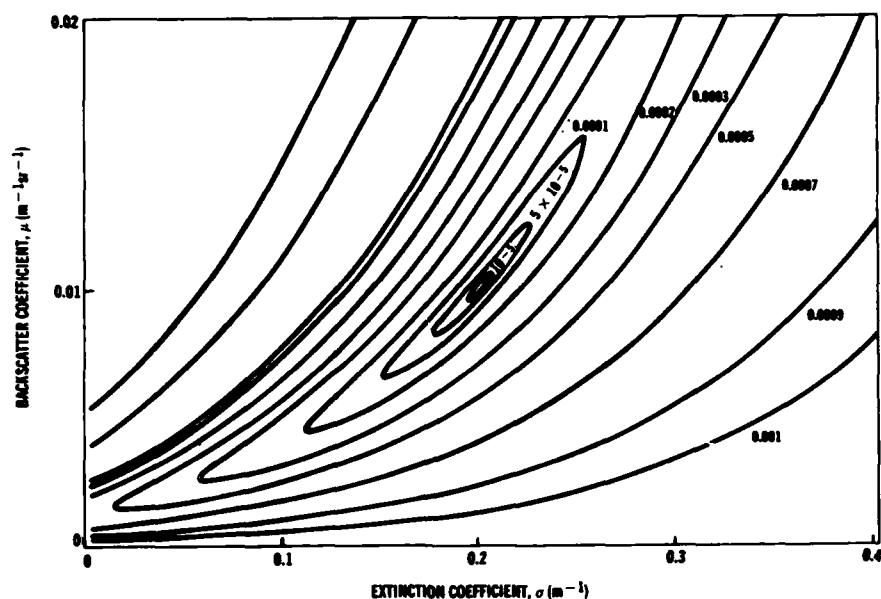


Figure 17. Constant-cost contours of  $J(\sigma, \mu) = [\Delta \text{Ph}(\sigma, \mu) - V]^T A [\Delta \text{Ph}(\sigma, \mu) - V]$  for  $A = \text{identity matrix}$  and for true values  $\sigma = 0.2 \text{ m}^{-1}$  and  $\mu = 0.01 \text{ m}^{-1} \text{sr}^{-1}$ ;  $h(\sigma, \mu)$  is column vector with components  $\mu e^{-\sigma c n} R(c n \Delta / 2)$  ( $n = 0, 1, \dots, 99$ ),  $\Delta = 1 \text{ ns}$ ,  $c = 0.3 \text{ m/ns}$ ,  $R$  is given by equation (29), and prime denotes transpose operation. Matrix  $P$  is defined by equation (26) with  $P(t)$  taken as in figure 9. Fixed  $J$ -values are shown next to contours.

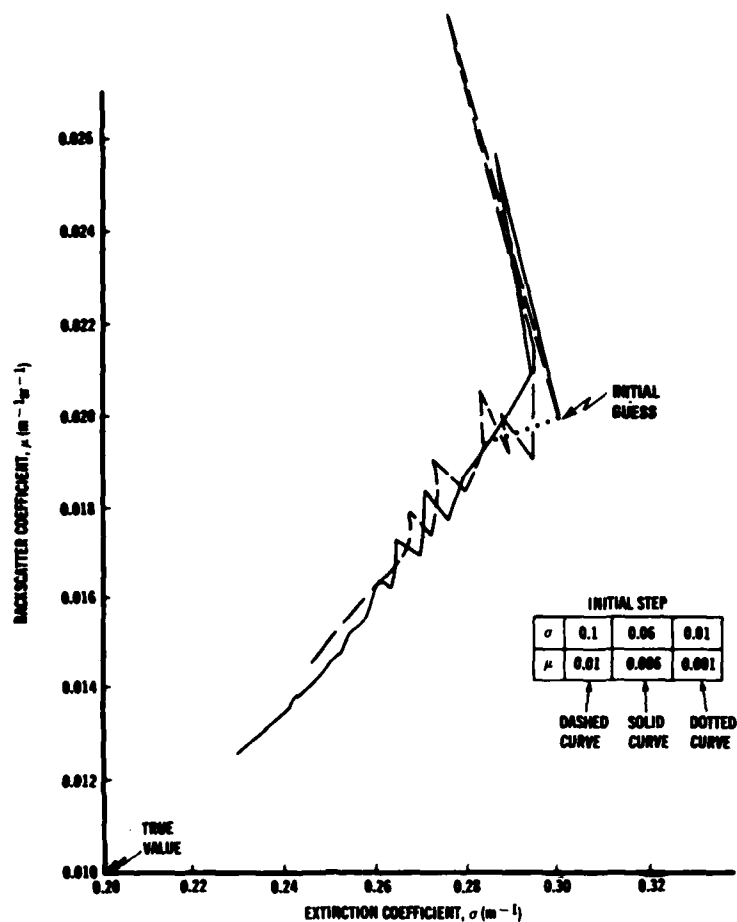


Figure 18. Typical trajectories for steepest descent algorithm with  $k_i = 1/i$ . True values are  $\sigma = 0.2 \text{ m}^{-1}$  and  $\mu = 0.01 \text{ m}^{-1}\text{sr}^{-1}$ , and initial guess was  $\sigma = 0.3 \text{ m}^{-1}$  and  $\mu = 0.02 \text{ m}^{-1}\text{sr}^{-1}$ . Several initial step sizes were used, and in each case 25 iterations of descent are shown.

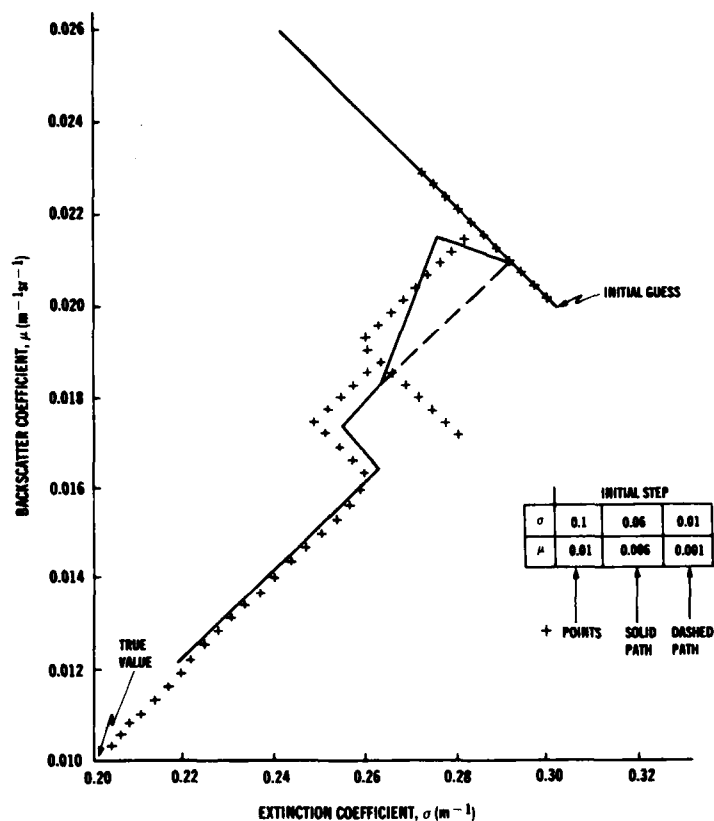


Figure 19. Typical trajectories for intuitive algorithm that adjusts  $\sigma$  and  $\mu$  at each step in accordance with comparison of peak values and decay times of  $\Delta\text{Ph}(\sigma, \mu)$  and true signal. True values and initial guess are as in example of figure 18. Results for several initial step sizes are shown; sequence  $\{1/i\}$  was used to scale corresponding iteration.

## 5.2 Estimation of $\sigma$ and $\mu$ from Measured Return Signals

To further investigate the utility of parameter estimation, the steepest-descent minimization procedure was applied to 10 samples of measured returns from cumulus clouds. These sample signals were taken from the HDL data collection (sect. 1) and were selected to correspond to measurements taken with the GaAs probe fully immersed in approximately uniform cloud, as determined by another instrument. The matrix  $A$  defining the cost function  $J$  of equation (54) was chosen to weight  $\Delta Ph(\sigma, \mu) - V$  in proportion to the measured signal value. This choice makes the model pulse  $\Delta Ph(\sigma, \mu)$  fit the measured one better where the signal level is high, thus deemphasizing the effect of measurement noise. The sequence  $\{k_i\}$  used to scale the descent was established empirically and has the form

$$k_i = C_1 / (20 + i) , \quad (56)$$

where the constant  $C_1$  is determined by normalization conditions.

Figure 20 (a to h) illustrates the results obtained for eight of the sample signals. The solid curves in these graphs represent  $\Delta Ph$  for the best-fit values of  $\sigma$  and  $\mu$ , and the dots show the sampled values of the measured return. The results for the remaining two sample signals gave negative best-fit values for  $\sigma$ . Closer examination of additional data characterizing the cloud regions that produced these signals revealed that the cloud distributions were decidedly nonuniform.

To determine the practicality of applying the foregoing approach to multilayer models needs further investigation. While there exist many computer routines for determining the extrema of functions of many variables, such routines are typically structured around a specific problem and might not be effective for other problems. An investigation of the structure of the M-layer analog of equation (54) together with a review of available minimization routines should clarify this issue.

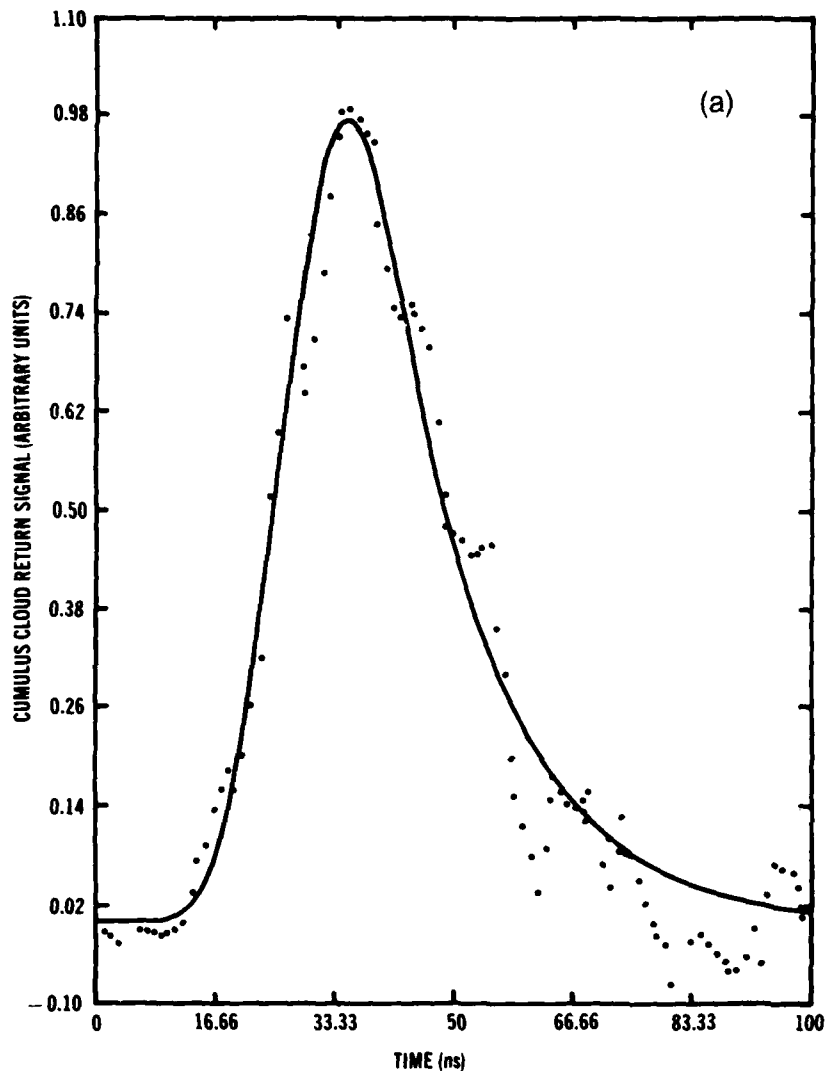


Figure 20. Sampled values of measured cumulus cloud return signal (dots) obtained with transmitter pulse of figure 1 and range-response curve of figure 3. Solid curves give  $\Delta Ph(\sigma, \mu)$  for best-fit values of  $\sigma$  and  $\mu$  determined by steepest-descent algorithm, where measurement system is assumed to have been fully immersed in uniform aerosol of unknown extinction and backscatter coefficients. Appropriate sampling of figure 1 transmitter pulse and equation (29) approximation of figure 3 range response was used for algorithm computations.

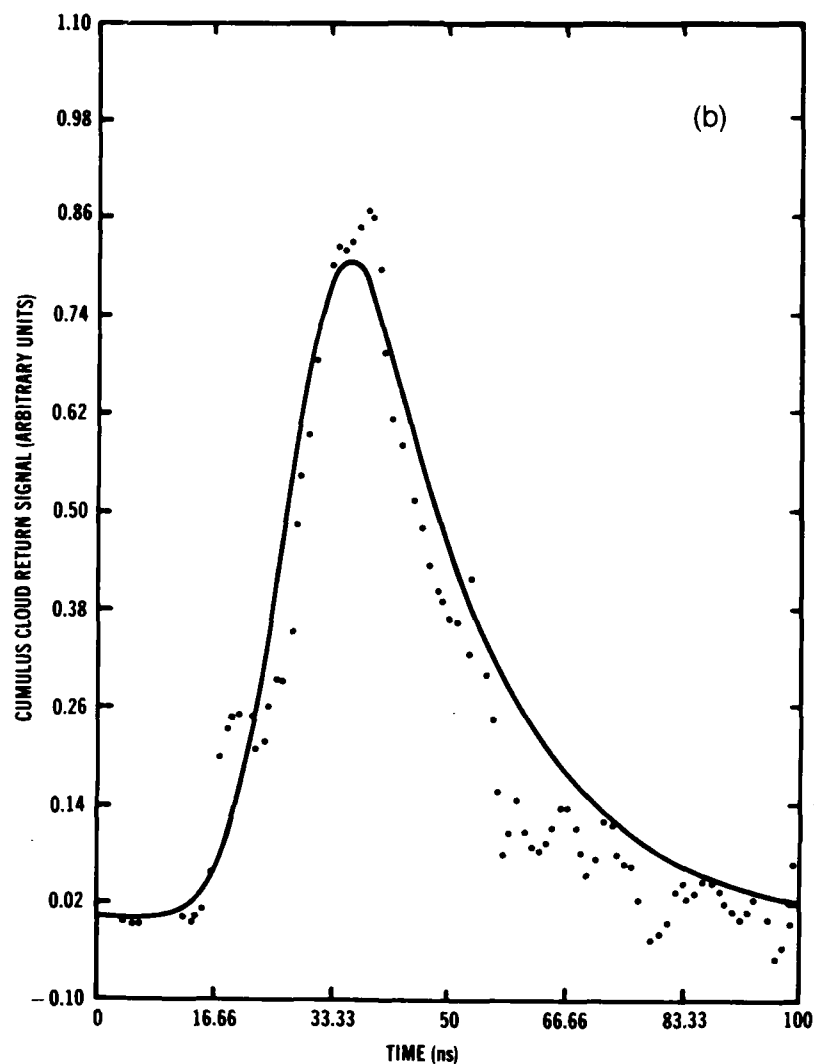


Figure 20 (Cont'd). Sampled values of measured cumulus cloud return signal (dots) obtained with transmitter pulse of figure 1 and range-response curve of figure 3. Solid curves give  $\Delta Ph(\sigma, \mu)$  for best-fit values of  $\sigma$  and  $\mu$  determined by steepest-descent algorithm, where measurement system is assumed to have been fully immersed in uniform aerosol of unknown extinction and backscatter coefficients. Appropriate sampling of figure 1 transmitter pulse and equation (29) approximation of figure 3 range response was used for algorithm computations.

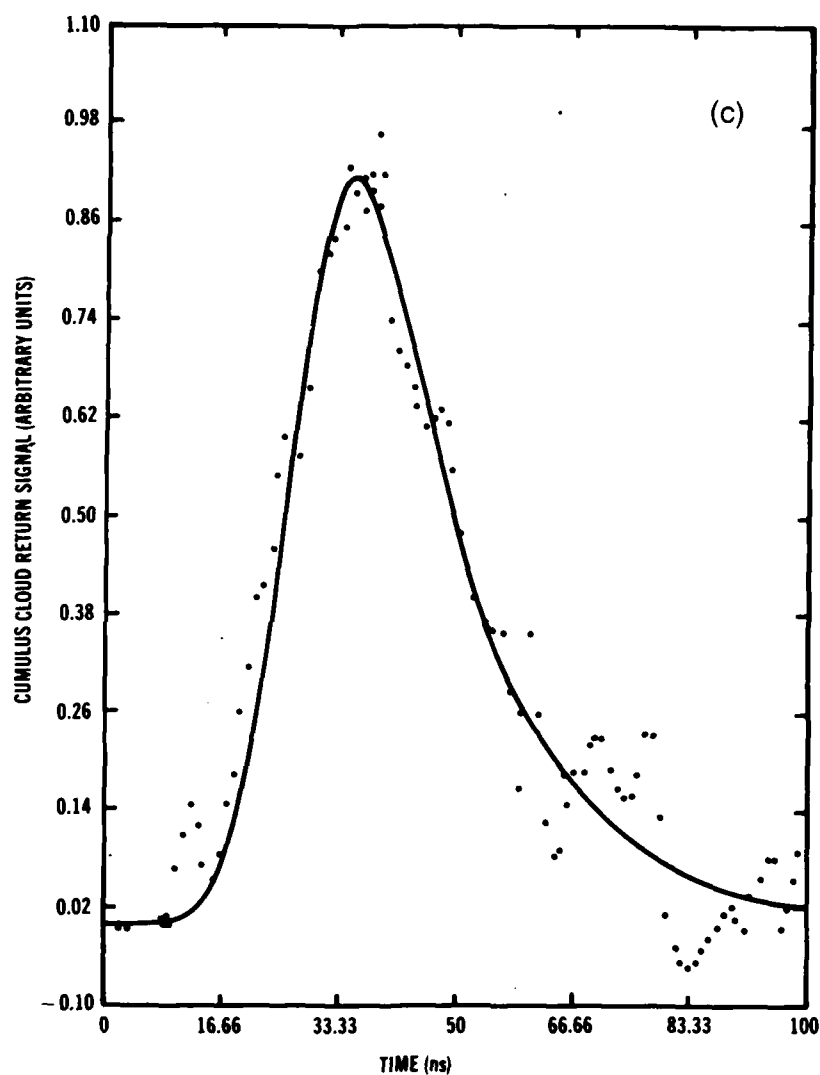


Figure 20 (Cont'd). Sampled values of measured cumulus cloud return signal (dots) obtained with transmitter pulse of figure 1 and range-response curve of figure 3. Solid curves give  $\Delta Ph(\sigma, \mu)$  for best-fit values of  $\sigma$  and  $\mu$  determined by steepest-descent algorithm, where measurement system is assumed to have been fully immersed in uniform aerosol of unknown extinction and backscatter coefficients. Appropriate sampling of figure 1 transmitter pulse and equation (29) approximation of figure 3 range response was used for algorithm computations.



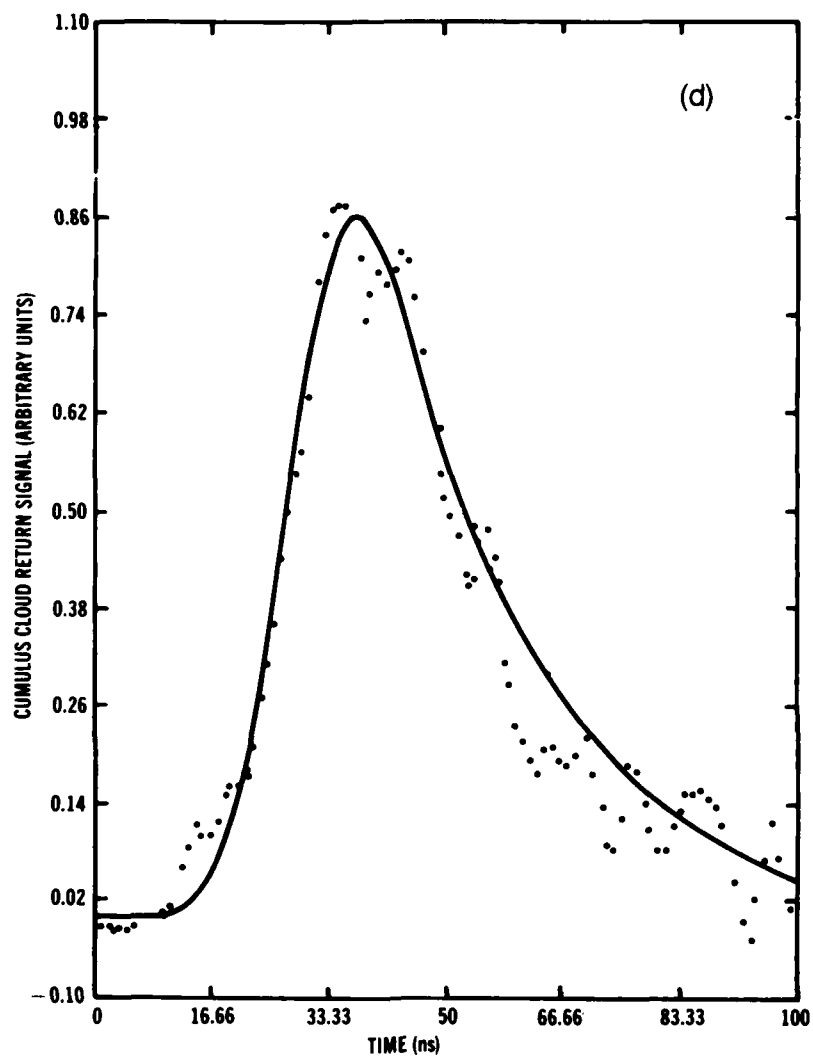


Figure 20 (Cont'd). Sampled values of measured cumulus cloud return signal (dots) obtained with transmitter pulse of figure 1 and range-response curve of figure 3. Solid curves give  $\Delta Ph(\sigma, \mu)$  for best-fit values of  $\sigma$  and  $\mu$  determined by steepest-descent algorithm, where measurement system is assumed to have been fully immersed in uniform aerosol of unknown extinction and backscatter coefficients. Appropriate sampling of figure 1 transmitter pulse and equation (29) approximation of figure 3 range response was used for algorithm computations.

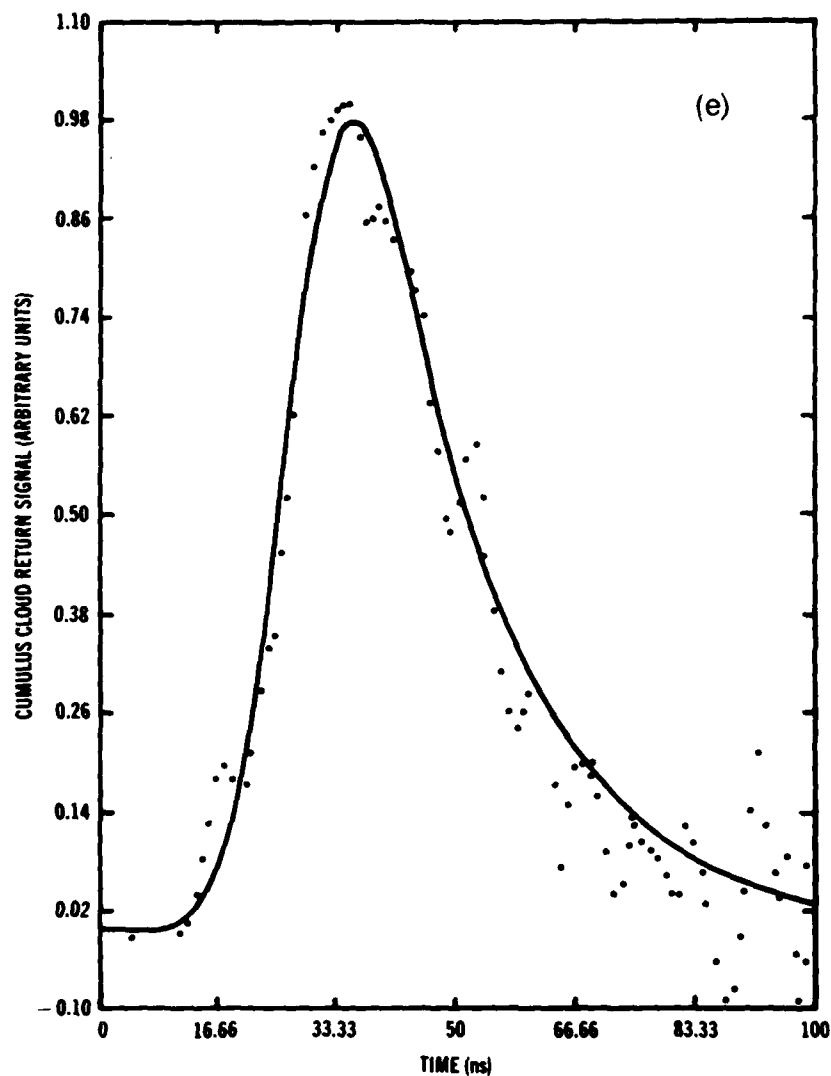


Figure 20 (Cont'd). Sampled values of measured cumulus cloud return signal (dots) obtained with transmitter pulse of figure 1 and range-response curve of figure 3. Solid curves give  $\Delta Ph(\sigma, \mu)$  for best-fit values of  $\sigma$  and  $\mu$  determined by steepest-descent algorithm, where measurement system is assumed to have been fully immersed in uniform aerosol of unknown extinction and backscatter coefficients. Appropriate sampling of figure 1 transmitter pulse and equation (29) approximation of figure 3 range response was used for algorithm computations.

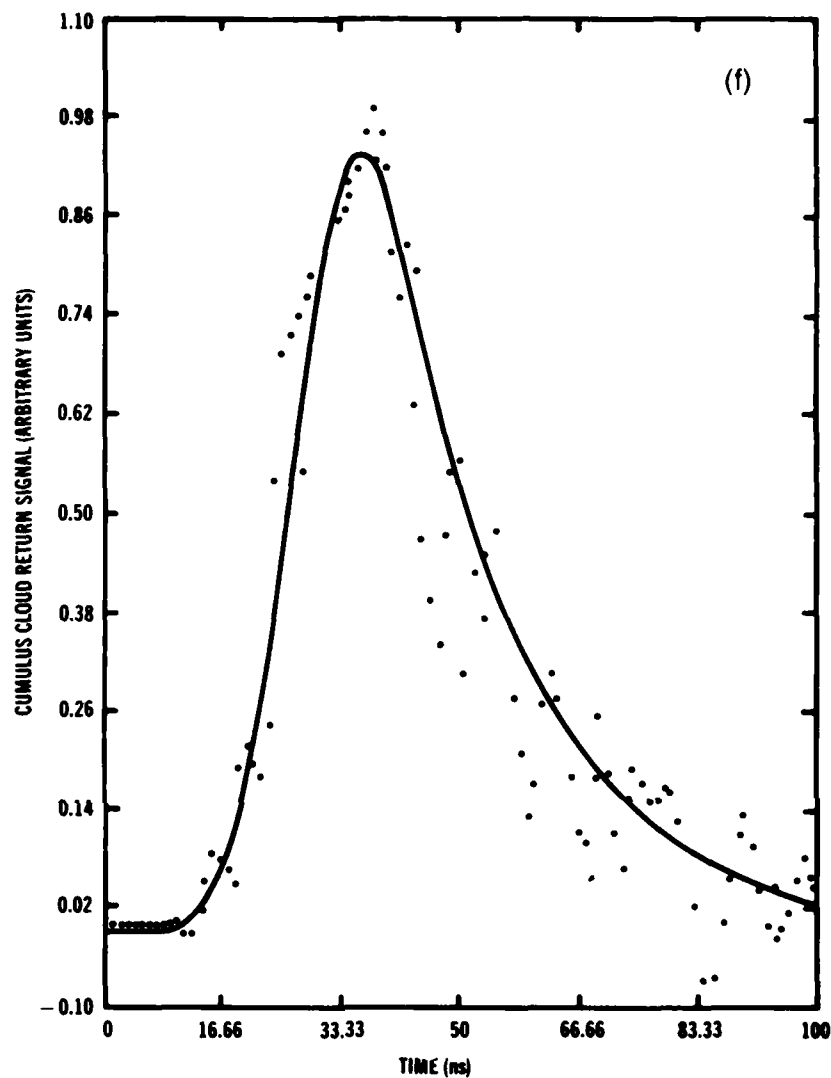


Figure 20 (Cont'd). Sampled values of measured cumulus cloud return signal (dots) obtained with transmitter pulse of figure 1 and range-response curve of figure 3. Solid curves give  $\Delta Ph(\sigma, \mu)$  for best-fit values of  $\sigma$  and  $\mu$  determined by steepest-descent algorithm, where measurement system is assumed to have been fully immersed in uniform aerosol of unknown extinction and backscatter coefficients. Appropriate sampling of figure 1 transmitter pulse and equation (29) approximation of figure 3 range response was used for algorithm computations.

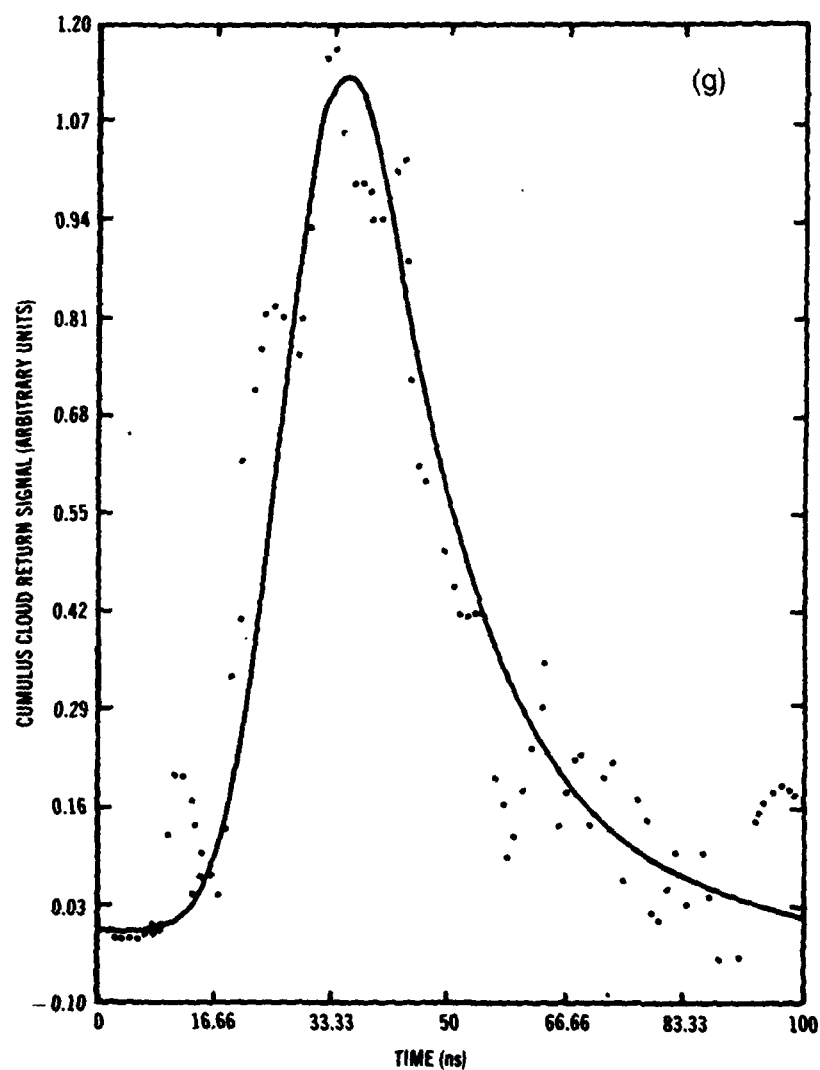


Figure 20 (Cont'd). Sampled values of measured cumulus cloud return signal (dots) obtained with transmitter pulse of figure 1 and range-response curve of figure 3. Solid curves give  $\Delta Ph(\sigma, \mu)$  for best-fit values of  $\sigma$  and  $\mu$  determined by steepest-descent algorithm, where measurement system is assumed to have been fully immersed in uniform aerosol of unknown extinction and backscatter coefficients. Appropriate sampling of figure 1 transmitter pulse and equation (29) approximation of figure 3 range response was used for algorithm computations.

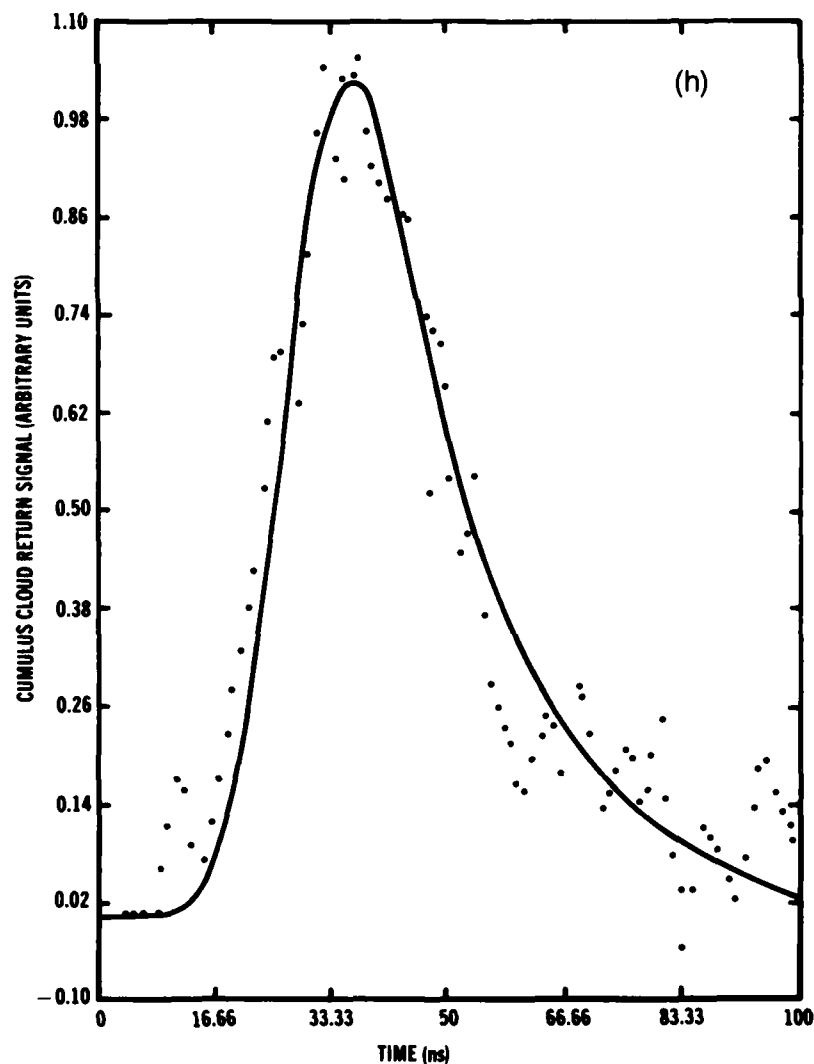


Figure 20 (Cont'd). Sampled values of measured cumulus cloud return signal (dots) obtained with transmitter pulse of figure 1 and range-response curve of figure 3. Solid curves give  $\Delta Ph(\sigma, \mu)$  for best-fit values of  $\sigma$  and  $\mu$  determined by steepest-descent algorithm, where measurement system is assumed to have been fully immersed in uniform aerosol of unknown extinction and backscatter coefficients. Appropriate sampling of figure 1 transmitter pulse and equation (29) approximation of figure 3 range response was used for algorithm computations.

## 6. SUMMARY AND DISCUSSION

This report discusses how a growing HDL data bank, consisting of measured backscattered laser pulses from aerosols such as weather clouds and smoke, must be treated before such data can be directly applied to evaluate the aerosol vulnerability of various AOF systems and methods for aerosol discrimination. The measurement system, a short-pulse GaAs laser probe, essentially convolves the features of the aerosol that are sought, namely, the aerosol signature, with the shape of the probe's transmitter pulse, after scaling the signature by the system's range-response characteristic. Thus deconvolution and rescaling are necessary to obtain the desired aerosol signatures.

Rescaling of the data using the known range-response characteristic of the probe is straightforward. Deconvolution with respect to the transmitter pulse, while possible in principle, is difficult to accomplish in practice, unless one is willing to accept the spatial resolution implied by the width of the probing pulses ( $\approx 2$  m). In the latter case, deconvolution reduces to a mere additional rescaling.

Two-meter spatial resolution is acceptable for most purposes, but is a serious drawback in attempting to gauge the buildup rates of aerosol density near the boundaries of an aerosol distribution. The deleterious effects of sharply rising aerosol edges on AOF system performance are likely the most difficult ones to cope with in designing an aerosol resistant system. It is therefore of great interest to obtain high-resolution measurements of aerosol signatures in regions where they may be changing rapidly.

In accepting the resolution implied by the width of the transmitter pulse, one assumes as an approximation that the transmitter pulse can be considered as a spatial  $\delta$ -function for the purpose of unraveling its convolution with the range-response scaled aerosol signature. This approximation results in the interpretation of the backscattered pulse as being proportional to the scaled aerosol signature, and in a roughly 2-m-resolution measurement. It is not necessary to make the foregoing approximate assumption, however. If the actual shape of the probing pulse is taken into account, the resulting convolution relation between the backscattered pulse and the aerosol signature not only is definite, but also is solvable for the signature, at least in principle. Consequently, increased resolution is theoretically possible through a more sophisticated interpretation of the data. The bulk of this report concerns the investigation and the development of this more sophisticated view. The findings and the results are summarized below.

It has been demonstrated that the mathematical process required to deconvolve backscattered pulses can be economically implemented on a computer. An algorithm that uses discrete Z-transform methods and is

ideally suited to the digital form of the backscatter data has been coded on computer and shown to be effective. Moreover, the running time of the program is sufficiently short to make the deconvolution of a large data bank feasible.

The essential difficulty in determining aerosol signatures by deconvolution is the effect of the noise present in the backscattered pulse measurements. A complete analysis of the effects of noise has been carried out and shows that the magnitude of noise errors in the aerosol signature depends sensitively on the noise spectrum in relation to the Fourier transform of the transmitter pulse. For example, if the latter vanishes at certain frequencies, and if the backscattered pulse's noise spectrum does not vanish sufficiently rapidly as these frequencies are approached, then the mean-squared noise level associated with the aerosol signature becomes infinite; that is, the SNR of the deconvolution-determined aerosol signature is zero. This catastrophic result can be avoided by appropriate filtering of the backscatter data prior to performing the deconvolution and does not occur at all if the Fourier transform,  $\hat{P}(f)$ , of the transmitter pulse does not vanish within the bandpass of the measurement system receivers. Moreover,  $\hat{P}(f)$  does not appear to vanish within the relevant bandpass, which is approximately 200 MHz, since a numerical Fourier transform of a typical measured transmitter pulse (fig. 2) showed no zeros for frequencies up to 250 MHz. However, backscatter data have been obtained with several distinct transmitter pulse shapes so that further analysis is required on this point.

The noise-effect analysis has been applied to the Fourier spectrum exhibited by the measured transmitter pulse of figure 2. The relationship between the SNR (peak signal divided by rms noise) of a backscattered pulse and that of the corresponding deconvolution-determined aerosol signature has thereby been determined (fig. 16). For the approximately 200-MHz receiver bandwidth, the results indicate that the SNR of the aerosol signature is 0.15 times the SNR of the backscattered pulse. To obtain reasonably good signature SNR's in the face of such a reduction factor requires a very good SNR for the backscatter measurement. Since the typical SNR for the backscatter measurements obtained with the transmitter pulse being considered is only about 15 to 1, we must conclude that the deconvolution method will fail to give acceptable results for these data.

Smoothing of the data has been considered as a way of improving the signature SNR; however, smoothing is tantamount to reducing the measurement bandwidth. The receiver bandwidth, which is actually somewhat greater than 200 MHz, results in a smearing of the received optical pulses by a spatial average over about a 0.5-m interval. We term this averaging interval the bandwidth resolution. Since 2-m resolution of

the aerosol signatures is already available without detailed deconvolution, there is no advantage in smoothing to a bandwidth resolution approaching 2 m. The effect of smoothing for the case in figure 16 can be seen by considering what would occur if the bandwidth were reduced to 150 MHz. Then the bandwidth resolution would worsen to about 1 m, while the signature SNR would be improved by only about 30 percent (fig. 16).

The most recent series of backscatter measurements has been made by using a shorter (5-ns FWHM), more symmetrical, and considerably higher peak-power transmitter pulse than that shown in figure 2. Typical SNR's for the backscattered pulses, while not yet determined accurately from the data, are expected to be 5 to 10 times greater than for previous measurements and therefore should make the deconvolution method more attractive. A noise analysis using the new transmitter pulse must still be made; but if the results are not too different from those for the pulse of figure 2, then signature SNR's approaching 20 to 1 may be obtainable.

Better signature extraction for the older data may be possible through an alternative approach. A preliminary investigation of using a priori knowledge about the signature--mainly its definition in terms of the physical parameters of the aerosol--and parameter estimation techniques has shown that excellent results can be obtained in simple cases (where the aerosol is known to be uniformly distributed and to completely engulf the measurement system). The method applies to all of the backscatter data presently available and, in addition, seems capable of providing more detailed information about the aerosol than is contained in its signature. The computational aspects of the method, however, are considerably more complex than those of direct deconvolution and may be difficult to implement for highly nonuniform aerosols.



#### LITERATURE CITED

- (1) D. McGuire, H. M. Smalley, and Z. G. Sztankay, Measurements of Backscatter Effects in Clouds at 0.9  $\mu\text{m}$  (U), Proc. JTCG/MD/WPFF Tri-Service Optical Fuze Technology Symposium, Naval Weapons Center NWC TP 5871, Part I (October 1976), 45-74. (CONFIDENTIAL)
- (2) Z. G. Sztankay and D. McGuire, Backscatter in Clouds at 0.9  $\mu\text{m}$  and Its Effects on Optical Fuzing Systems (U), Proc. Seventh DoD Conference on Laser Technology (November 1977). (SECRET)
- (3) Z. G. Sztankay, Measurement of the Localized Optical Characteristics of Natural Aerosols, Smoke, and Dust, Proc. Smoke/Obscurants Symposium II (25-26 April 1979).
- (4) Jonathan Vanderwall and Michael Conner, A Novel Scan-Converting Oscillographic Technique for In-Situ Signal Acquisition with Subsequent Automatic Digitization, Harry Diamond Laboratories HDL-TR-1956 (1981).
- (5) H. H. Burroughs, Computation of Cloud Backscatter Power as a Function of Time for an Active Optical Radar (U), Naval Weapons Center NWC TP 5090 (April 1971). (CONFIDENTIAL)
- (6) Jonathan Vanderwall, Walter V. Hattery, and Zoltan G. Sztankay, Subnanosecond Rise Time Injection Laser Pulses, Harry Diamond Laboratories HDL-TR-1697 (March 1975).
- (7) E. I. Jury, *Theory and Application of the Z-transform Method*, John Wiley & Sons, Inc., New York (1964).
- (8) A. Sage and J. Melsa, *System Identification*, Academic Press, Inc., New York (1971).

## DISTRIBUTION

ADMINISTRATOR  
DEFENSE TECHNICAL INFORMATION CENTER  
ATTN DTIC-DDA (12 COPIES)  
CAMERON STATION, BUILDING 5  
ALEXANDRIA, VA 22314

COMMANDER  
US ARMY RSCH & STD GP (EUR)  
PO BOX 65  
ATTN CHIEF, PHYSICS & MATH BRANCH  
FPO NEW YORK 09510

COMMANDER  
US ARMY ARMAMENT MATERIEL  
READINESS COMMAND  
ATTN DRSAR-LEP-L, TECHNICAL LIBRARY  
ROCK ISLAND, IL 61299

COMMANDER  
US ARMY MISSILE & MUNITIONS  
CENTER & SCHOOL  
ATTN ATSK-CTD-F  
REDSTONE ARSENAL, AL 35809

DIRECTOR  
US ARMY MATERIEL SYSTEMS ANALYSIS ACTIVITY  
ATTN DRXSX-MP  
ABERDEEN PROVING GROUND, MD 21005

DIRECTOR  
US ARMY BALLISTIC RESEARCH LABORATORY  
ATTN DRDAR-TSB-S (STINFO)  
ABERDEEN PROVING GROUND, MD 21005

TELEDYNE BROWN ENGINEERING  
CUMMINGS RESEARCH PARK  
ATTN DR. MELVIN L. PRICE, MS-44  
HUNTSVILLE, AL 35807

ENGINEERING SOCIETIES LIBRARY  
345 EAST 47TH STREET  
ATTN ACQUISITIONS DEPARTMENT  
NEW YORK, NY 10017

HQ, USAF/SAMI  
WASHINGTON, DC 20330

US ARMY ELECTRONICS TECHNOLOGY  
& DEVICES LABORATORY  
ATTN DELET-DD  
FT MONMOUTH, NJ 07703

COMMANDER  
US ARMY ARMAMENT RESEARCH  
& DEVELOPMENT COMMAND  
ATTN DRDAR-SE, SYSTEMS EVALUATION  
OFFICE, LTC GRADY COOK  
ATTN DRDAR-LCN-C, G. TAYLOR  
ATTN DRDAR-AS, R. ANDREJZOVICS  
DOVER, NJ 07801

DIRECTOR  
NIGHT VISION & ELECTRO-OPTICS  
LABORATORY  
ATTN DELNV-V (2 COPIES)  
ATTN DELNV-R, R. BUSER  
FT BELVOIR, VA 22060

COMMANDER/DIRECTOR  
ATMOSPHERIC SCIENCES LABORATORY  
ATTN DELAS-EO, F. NILES  
WHITE SANDS MISSILE RANGE, NM 88002

COMMANDER  
US ARMY MISSILE COMMAND  
ATTN DRSMI-REM, H. ANDERSON  
REDSTONE ARSENAL, AL 35898

ENVIRONMENTAL RESEARCH INSTITUTE  
OF MICHIGAN  
PO BOX 618  
ATTN IRIA LIBRARY  
ANN ARBOR, MI 48107

COMMANDER  
NAVAL WEAPONS CENTER  
ATTN CODE 3311, K. BULLOCK (4 COPIES)  
ATTN CODE 3331, J. CRISLER  
CHINA LAKE, CA 93555

COMMANDER  
AFATL  
ATTN L. STABLES  
EGLIN AIR FORCE BASE, FL 32542

COMMANDER  
AFAL/TEO  
ATTN R. HARRIS  
WRIGHT-PATTERSON AF BASE, OH 45433

MOTOROLA, INC  
GOVERNMENT ELECTRONICS DIVISION  
ATTN A. GARAS (2 COPIES)  
PO BOX 1417  
8201 E MCDOWELL RD  
SCOTTSDALE, AZ 85252

DISTRIBUTION (Cont'd)

SANTA BARBARA RESEARCH CENTER  
ATTN N. RIGBY (2 COPIES)  
75 COROMAR DRIVE  
GOLETA, CA 93117

US ARMY ELECTRONICS RESEARCH  
& DEVELOPMENT COMMAND  
ATTN TECHNICAL DIRECTOR, DRDEL-CT  
ATTN LEGAL OFFICE

HARRY DIAMOND LABORATORIES  
ATTN CO/TD/TSO/DIVISION DIRECTORS  
ATTN RECORD COPY, 81200  
ATTN HDL LIBRARY, 81100 (3 COPIES)  
ATTN HDL LIBRARY, 81100 (WOODBIDGE)  
ATTN TECHNICAL REPORTS BRANCH, 81300  
ATTN CHAIRMAN, EDITORIAL COMMITTEE  
ATTN MORRISON, R., 13500 (GIDEP)  
ATTN CHIEF, 13000  
ATTN CHIEF, 11000  
ATTN CHIEF, 13300  
ATTN CHIEF, 11400  
ATTN COX, L, 00211  
ATTN HUMPHREY, R., 13300  
ATTN GRIFFIN, J. , 21100  
ATTN VANDERWALL, J., 12300  
ATTN SANN, K. H., 15000  
ATTN PEPERONE, S., 42600  
ATTN DOBRIANSKY, B., 13500 (2 COPIES)  
ATTN LANHAM, C., 00210  
ATTN GIGLIO, D., 15300  
ATTN GEIPE, T., 22100  
ATTN TUTTLE, J., 21400  
ATTN CONNER, M., 15200  
ATTN MCGUIRE, D., 13300 (10 COPIES)

